Geofluids (2002) **2**, 63–94

Ancient hydrocarbon seeps from the Mesozoic convergent margin of California: carbonate geochemistry, fluids and palaeoenvironments

K. A. CAMPBELL[1], J. D. FARMER[2] AND D. DES MARAIS[3]

[1]Geology Department, University of Auckland, Auckland, New Zealand; [2]Geology Department, Arizona State University, Tempe, AZ, USA; [3]NASA Ames Research Center, Moffett Field, CA, USA

ABSTRACT

More than a dozen hydrocarbon seep-carbonate occurrences in late Jurassic to late Cretaceous forearc and accretionary prism strata, western California, accumulated in turbidite/fault-hosted or serpentine diapir-related settings. Three sites, Paskenta, Cold Fork of Cottonwood Creek and Wilbur Springs, were analyzed for their petrographic, geochemical and palaeoecological attributes, and each showed a three-stage development that recorded the evolution of fluids through reducing–oxidizing–reducing conditions. The first stage constituted diffusive, reduced fluid seepage (CH_4, H_2S) through seafloor sediments, as indicated by Fe-rich detrital micrite, corroded surfaces encrusted with framboidal pyrite, anhedral yellow calcite and negative cement stable isotopic signatures ($\delta^{13}C$ as low as −35.5‰ PDB; $\delta^{18}O$ as low as −10.8‰ PDB). Mega-invertebrates, adapted to reduced conditions and/or bacterial chemosymbiosis, colonized the sites during this earliest period of fluid seepage. A second, early stage of centralized venting at the seafloor followed, which was coincident with hydrocarbon migration, as evidenced by nonluminescent fibrous cements with $\delta^{13}C$ values as low as −43.7‰ PDB, elevated $\delta^{18}O$ (up to +2.3‰ PDB), petroleum inclusions, marine borings and lack of pyrite. Throughout these early phases of hydrocarbon seepage, microbial sediments were preserved as layered and clotted, nondetrital micrites. A final late-stage of development marked a return to reducing conditions during burial diagenesis, as implied by pore-associated Mn-rich cement phases with bright cathodoluminescent patterns, and negative $\delta^{18}O$ signatures (as low as −14‰ PDB). These recurring patterns among sites highlight similarities in the hydrogeological evolution of the Mesozoic convergent margin of California, which influenced local geochemical conditions and organism responses. A comparison of stable carbon and oxygen isotopic data for 33 globally distributed seep-carbonates, ranging in age from Devonian to Recent, delineated three groupings that reflect variable fluid input, different tectono-sedimentary regimes and time–temperature-dependent burial diagenesis.

Key-words: ancient hydrocarbon seeps, California Mesozoic, carbonate geochemistry, carbonate paragenesis, stable isotopes

Received 23 June 2001; accepted 8 November 2001

Corresponding author: Kathleen A. Campbell, Geology Department, University of Auckland, Private Bag 92019, Auckland, New Zealand.
E-mail: ka.campbell@auckland.ac.nz. Tel: +64 9 373 7599, ext. 7418. Fax: +64 9 373 7435.

Geofluids (2001) **2**, 63–94

INTRODUCTION

Modern hydrocarbon seeps and hydrothermal vent environments (Fig. 1) are situated at distinctive geotectonic, geochemical and biological interfaces where H_2S- and CH_4-rich fluids are discharged at the seafloor, sustaining lush chemosynthetic ecosystems. Modern vent-seep biota are dominated by chemoautotrophic microbes, and recurring assemblages of sulphide-tolerant mega-invertebrates, some with endosymbiotic bacteria (reviewed in Van Dover 2000). Chemosynthetic bacteria oxidize vent-seep fluids, which are generated along plate boundaries (oceanic spreading centres, subduction zones), or where faulting, diapirism or undersea landslides tap organic-rich porewaters (e.g. Humphris *et al.* 1995; Langseth & Moore 1990; Schumacher & Abrams 1996). Authigenic precipitates form from vent-seep fluids, ranging from metal-rich, sulphate–sulphide–silica deposits at high-temperature vent sites (~200–400°C), to carbonates at hydrocarbon seep

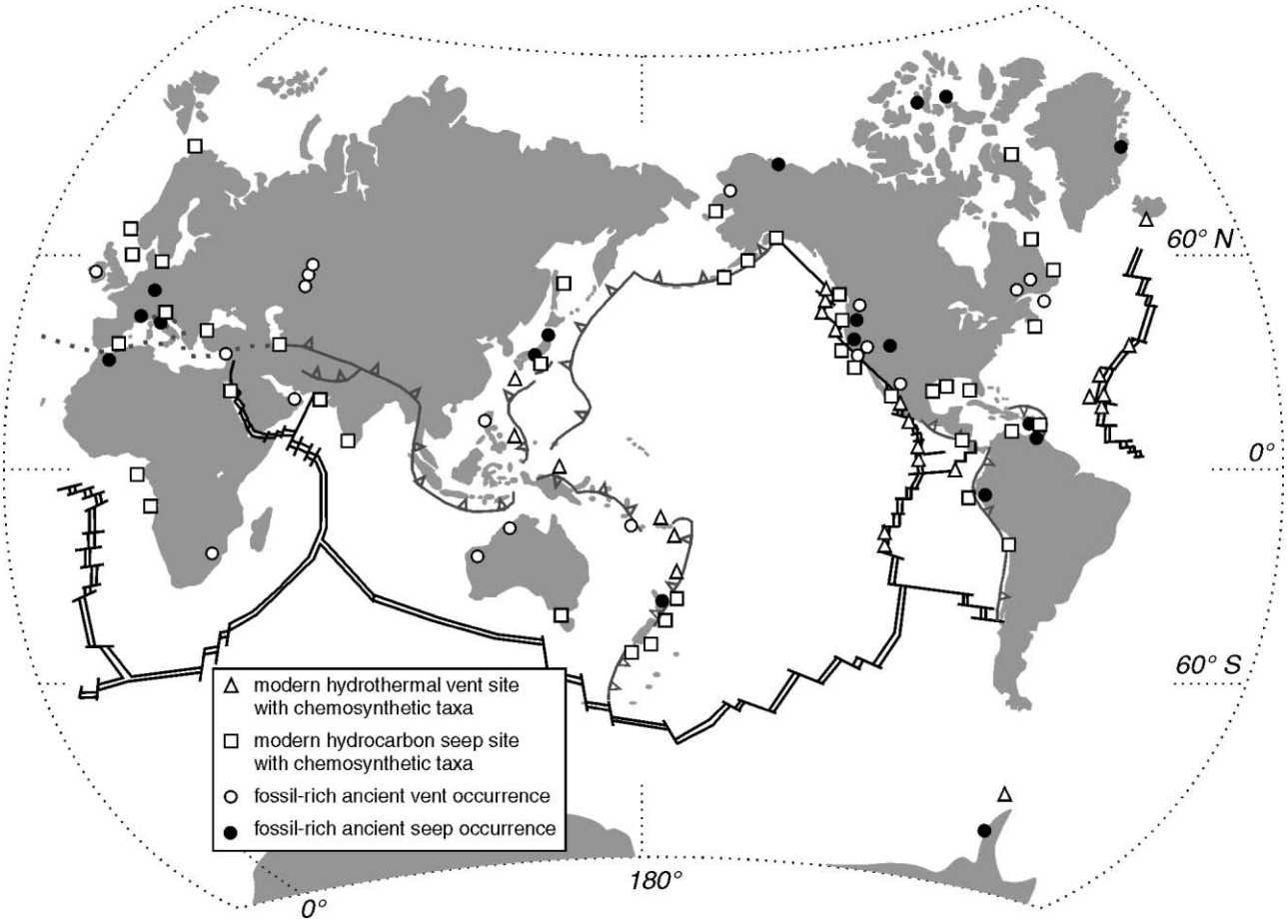

Fig. 1. World-wide distribution map of modern and ancient (Archaean to recent) hydrothermal vent and hydrocarbon seep occurrences with chemosynthetic community associations. Plate boundary symbols include: double line, constructive; tooth pattern, destructive; single line, strike–slip. Data compiled from numerous literature sources (e.g. Campbell & Bottjer 1995a; Hovland & Judd 1988; Little *et al*. 2002; Van Dover 2000).

sites with near-ambient bottom water temperatures (e.g. Hannington *et al.* 1995; Ritger *et al.* 1987).

Ancient hydrocarbon seep and hydrothermal vent deposits of Early Archaean to Quaternary age have been reported from ore deposits and marine sedimentary sequences world-wide (Fig. 1) (e.g. Campbell & Bottjer 1995a; de Ronde & Ebbesen 1996). Microorganisms have occupied marine hydrothermal vent settings since the Precambrian (e.g. 3.2 Ga, de Ronde & Ebbesen 1996; 2.2 Ga, Rasmussen 2000), and mega-invertebrates have existed in volcanic vent deposits since at least the Silurian (Little *et al.* 1997). Seep-carbonates with abundant mega-fossils have been recognized in sedimentary rocks as old as Devonian (Peckmann *et al.* 2000). Criteria used to identify vent-seep deposits in the geological record are described in detail elsewhere (Aharon 1994, 2000; Beauchamp *et al.* 1989; Campbell & Bottjer 1995a; Cavagna *et al.* 1999; Gaillard *et al.* 1992; Little *et al.* 1998; Peckmann *et al.* 1999a). In general, vent-seep deposits are recognized by their structural and stratigraphic associations, their distinctive mineralogical and geochemical features, and their body fossil, textural or molecular biomarker signatures indicative of chemosynthetic organism activity. In particular, the paragenetic sequence of cement/mineral phases within vent or seep deposits provides a temporal–spatial context for the geochemical assessment of whether the fuels for chemosynthesis (e.g. H_2S, CH_4) were present and contemporaneous with organism activity (cf. Cook & Stakes 1995). Moreover, within the context of well-defined paragenetic sequences, the isotopic and elemental geochemistry of discrete fabric types and mineral phases can be used to trace the changing fluid-diagenetic pathways of an ancient vent or seep deposit within its larger geotectonic and geohydrological framework (cf. Sample 1996; Sample *et al.* 1993).

To date, more than a dozen Upper Jurassic to Upper Cretaceous (Tithonian–Campanian) hydrocarbon seep-carbonate occurrences have been recognized in forearc strata (Great Valley Group) and accretionary prism rocks (Franciscan Group) of northern and central California (Fig. 2). The present study

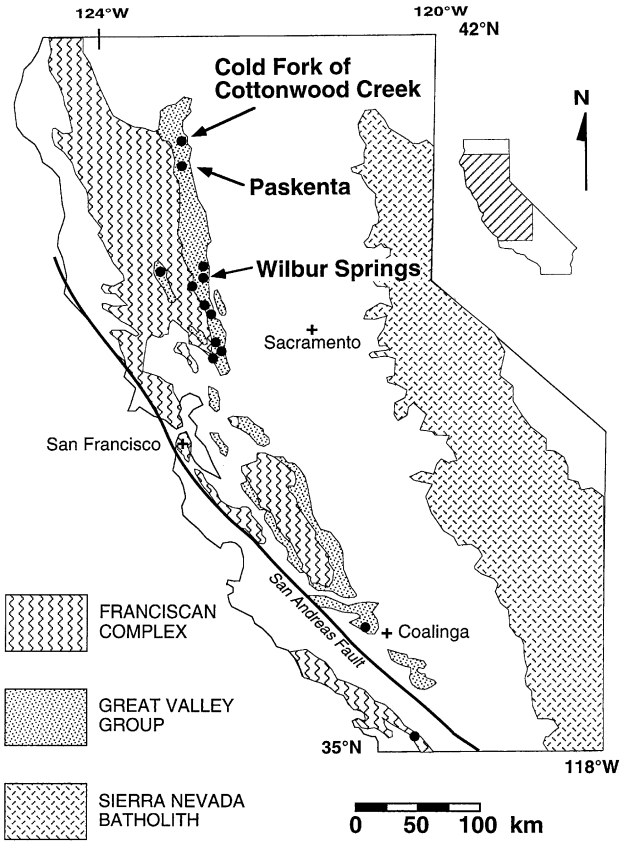

Fig. 2. Geotectonic and location map for Mesozoic seep-carbonate deposits (filled circles) of western California. The three seep-carbonate occurrences of this study include the Cold Fork of Cottonwood Creek, Paskenta and Wilbur Springs localities. Simplified geology of north–south-trending convergent margin system includes, from west to east: Franciscan Accretionary Complex (Jurassic to Cretaceous) – belts of mélange, broken formation and tectonic slivers of oceanic crust substratum; Great Valley Group (Jurassic to Palaeogene) – siliciclastic forearc turbidites; and Sierra Nevada batholith – present-day roots of Mesozoic volcanic arc. Blank areas indicate rock types or alluvium unrelated to this study.

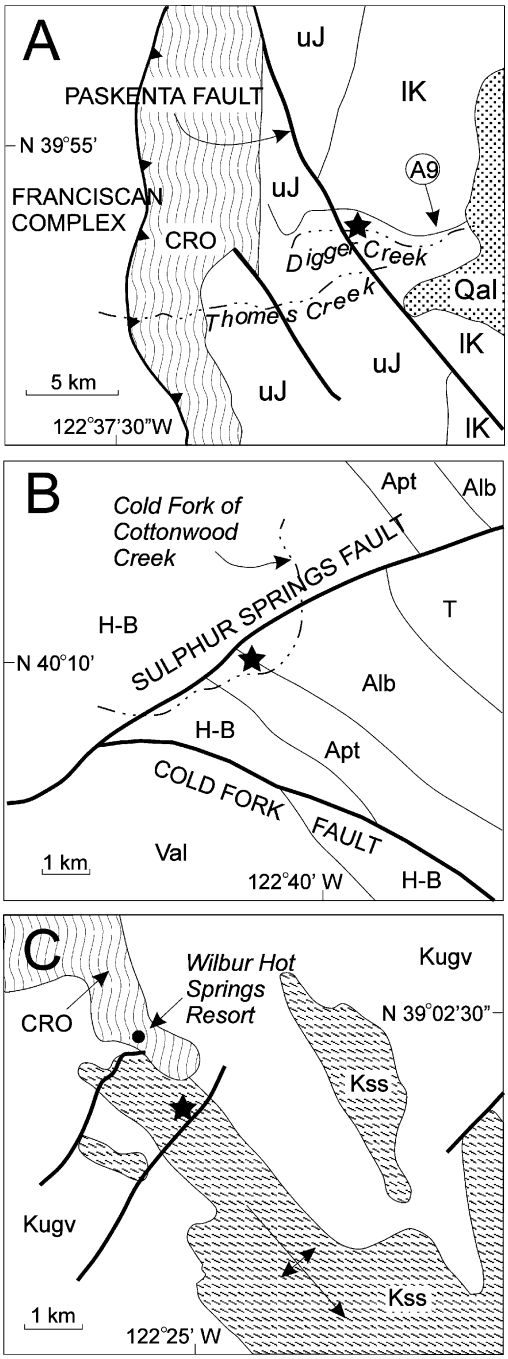

Fig. 3. Geology of the three seep-carbonate deposits (stars) of this study. (A) The Paskenta deposit (Tithonian) is situated within a synsedimentary, listric fault zone (Paskenta Fault). Compare with field photograph (Fig. 4A). uJ, IK = Upper Jurassic, Lower Cretaceous. Geology modified from Jones *et al*. (1969). (B) The Cold Fork of Cottonwood Creek site (Albian–Aptian) is situated near the junction of the synsedimentary Cold Fork and Sulphur Springs Faults. Val = Valanginian; H–B = Hauterivian–Barremian; Alb = Albian; Apt = Aptian; T = Tertiary. Map and ages of stratigraphic units modified from Bailey & Jones (1973). (C) The Wilbur Springs deposit (Hauterivian) occurs in diapir-associated sedimentary serpentinites (Kss) affiliated with the Coast Range Ophiolite (CRO). Kugv = Cretaceous, undifferentiated Great Valley Group turbidites. Map simplified from Carlson (1984c).

is the first to provide an integrated view of the sedimentology, paragenesis and geochemistry of three of these seep-carbonates as a context for their palaeoecological and palaeoenvironmental development. The Paskenta (Tithonian, Upper Jurassic), Wilbur Springs (Hauterivian, Lower Cretaceous) and Cold Fork of Cottonwood Creek (Albian–Aptian, Lower Cretaceous) seep deposits (Fig. 2), northern California, were chosen for detailed study because they span a considerable portion of the 70 Myr history of fluid seepage and contemporaneous marine sedimentation in the Great Valley forearc. In addition, the deposits formed in either of the two known types of tectono-sedimentary regimes that generated hydrocarbon seepage along this ancient convergent margin – synsedimentary fault-associated turbidites, and serpentine diapir-related settings (Fig. 3; Campbell *et al.* 1993). The fossil fauna of the three localities also recorded part of an evo-

lutionary transition in vent-seep benthos world-wide (Campbell & Bottjer 1995a), yet the enclosing seep-carbonates had not, until this study, been analyzed for their geochemical and palaeoenvironmental attributes.

GEOLOGICAL AND PALAEONTOLOGICAL CONTEXT OF STUDY SITES

The tectonic significance of the Great Valley Group, western California, as a deep marine forearc basin was recognized in the early years of plate tectonic reconstruction of continental geology (Dickinson 1971; Ernst 1970; Hamilton 1969). Strata up to 15 km thick constitute mostly siliciclastic turbidites that were deposited from the late Jurassic to the Palaeogene, in a north–south axial forearc basin (Ingersoll & Dickinson 1981). The petrofacies and tectono-chronological links among the forearc basin (Great Valley Group), accretionary wedge (Franciscan Complex) and magmatic arc (Sierra Nevada batholith) are now well-established (Ingersoll 1983). In places along the western margin of their outcrop extent, Great Valley forearc strata and structural slivers of the oceanic crust substratum (Coast Range Ophiolite) were tectonically juxtaposed above the coeval, highly deformed and metamorphozed Franciscan subduction complex (e.g. Bailey *et al.* 1964; Dickinson *et al.* 1996).

For many years, isolated pods and lenses of anomalous 'white limestones' with abundant mega-fossils were known from the otherwise fossil-poor Great Valley turbidites (e.g. Anderson 1945; Berkland 1973; Campbell *et al.* 1993; Carlson 1984a; Gabb 1869; Lawton 1956; Stanton 1895) (Fig. 2). Before it was understood that the enclosing siliciclastic strata had deep-water, offshore origins, most early investigators assigned these stratigraphically restricted carbonate lenses to shallow reef palaeoenvironments. Spectacular gastropod and brachiopod coquinas from these carbonates are noteworthy (e.g. Campbell 1996; Campbell & Bottjer 1995b; Klosterman *et al.* 2001; Sandy & Campbell 1994). Also abundant are masses of worm tubes and fossil representatives of solemyid, lucinid, thyasirid and mytilid bivalves (including mussels up to 25 cm in length), which are now recognized to be related to living chemosymbiotic groups (Campbell *et al.* 1993).

Turbidite-hosted deposits predominate among the documented Mesozoic seep-carbonates of California. They collectively represent diachronous fluid migration and localized fluid expulsion in an evolving forearc basin, from the Late Jurassic (Tithonian) to the Late Cretaceous (Campanian). Examples from this study include both the Paskenta and Cold Fork of Cottonwood Creek limestone deposits, which occur along large-scale, north-east-trending, regional structural features (Paskenta and Sulphur Springs Faults, respectively; Fig. 3A,B). Suchecki (1984) and Moxon (1990) used regional structural and stratigraphic relations to infer a listric, normal geometry for these and other similar faults active during the sedimentation of Great Valley strata. Faults offered flow pathways for both hydrocarbon-charged fluids generated within the sedimentary prism and fluid contributions from greater depth. When considered within the overall tectono-stratigraphic context for the Late Mesozoic arc–trench system, the turbidite-hosted, Great Valley seep-carbonates formed more or less continuously, in patchy distributions along strike for ~500 km (Fig. 2), during a time span of at least 70 Myr of forearc subduction history.

Sedimentary serpentinites, or foliate serpentinite breccias, host seep-carbonates of the Wilbur Springs area, the third study site (Fig. 3C), which are part of an unusual, temporally and spatially restricted tectonic event of the Early Cretaceous (Hauterivian to Albian). This event represents entertainment and subsequent expulsion in seafloor serpentine diapirs of both high-pressure metamorphic blocks and deeply originated fluids from the subjacent oceanic crust (Coast Range Ophiolite; Campbell *et al.* 1993; Carlson 1984a). The serpentinite exposed at Wilbur Springs is an example of a submarine extrusion, possibly a seamount (Campbell *et al.* 1993), and is analogous to the extensional field of serpentine mud volcanoes, seamounts and seep-carbonate chimneys found today in the outer Marianas forearc basin (Fryer 1992; Haggerty 1987, 1991). The Wilbur Springs carbonates of this study likely formed where seeps occurred atop or on the flanks of the source protrusion, as fluids exuded from the diapir breaching the seafloor (Campbell *et al.* 1993). Subsequently, the carbonates were rafted away from the source protrusion by mobile serpentinite flows that advanced eastward to interfinger with terrigenous turbidites along the axial floor of the forearc basin (Campbell *et al.* 1993; Carlson 1984a).

METHODS OF STUDY

Standard thin sections were examined by plane-polarized, cross-polarized, UV and reflected light microscopy. Cathodoluminescence (CL) was generated by a Cambridge luminoscope system (10–13 kV, 500 μA). CL maps were constructed of representative thin sections to aid in the selection of spot-sample transects for elemental analysis. Carbonate cements were stained with alizarin red and Feigl's solution (Lewis & McConchie 1994) to differentiate among mineral phases. Rock-chip preparation for stable isotope analysis included sonication in distilled water, oven drying and microdrilling of samples under a binocular microscope. Powdered samples were weighed (150–400 mg) and roasted *in vacuo* at 375°C for 1 h. CO_2(g) was evolved from each sample by reaction with orthophosphoric acid (90°C), and analyzed in an automated carbonate device attached to a VG Prism II stable isotope ratio mass spectrometer at the University of Southern California (USC). To remove SO_2(g) in sulphide-rich carbonate, micrite powders were run offline at North Carolina State University (NCSU) on a Finnigan MAT 251 ratio mass

spectrometer, after the CO_2(g) had been passed through a variable temperature trap (−120°C). Weighed internal laboratory standards were interspersed with samples and analyzed during the runs. For both carbon and oxygen, laboratory precision was better than 0.1‰ (USC) and 0.06‰ (NCSU).

In situ elemental analyses of carbon-coated, polished thin sections were performed on a Cameca SX-51 wavelength dispersive (WDS) electron probe microanalyzer at the University of California, Berkeley (UCB). Operating conditions were as follows: take-off angle, 40.0°; width of defocused beam, 20 µm; beam voltage, 20 kV; beam current, 50 nA; count times for majors/traces, 160/320 s. To determine the precision and detection limits during microprobe runs, multiple beam spots were analyzed on a standard calcite (UCB #135) under the same operating conditions as the unknowns. The accuracy of measurements was improved by correction of offsets acquired during standard runs, in accordance with measured elemental abundance on the standard calcite (by inductively coupled plasma-mass spectrometry (ICP-MS), X-ray fluorescence-energy dispersive spectroscopy (XRF-EDS)). Online data acquisition and reduction were performed by Probe for Windows® software, with an empirical technique applied to improve interference corrections for trace element analyses (Donovan *et al.* 1993) – the Bence–Albee α-factor correction (polynomial fit) as modified by Armstrong (1988). In addition, the software calculated CO_3^{2} – content based on a one-to-one atom of Ca, and corrected the measurements of the other elements for the matrix effect of the carbonate ion, further improving accuracy. Moreover, X-ray intensities were corrected for beam drift, count time, standard count drift, spectral interference, off-peak backgrounds (linear interpolation) and pulse height analysis.

RESULTS OF FIELD STUDIES

Detailed outcrop descriptions of the Paskenta, Cold Fork of Cottonwood Creek and Wilbur Springs localities can be found in Campbell & Bottjer (1993, 1995b), Campbell *et al.* (1993) and Campbell (1995). In the field, seep-carbonates occurred in isolated pods or lenses (e.g. Fig. 4A), which generally were divisible into two broad types (e.g. Fig. 4B,C): (i) dark microcrystalline calcite (micrite), containing fossils and detrital grains; and (ii) various lighter coloured, layered cements. Commonly, these two carbonate types were spatially separated by irregular, pyrite-coated corrosion surfaces (Fig. 4C). Cavities (millimetre to decimetre scale) were common (Fig. 4C), with a fill of internal silt-clay, peloidal geopetals or blocky, clear spar. In addition, small (up to a few centimetres in diameter), nodular masses of micritic carbonate could be traced laterally into the enclosing siliciclastics for short distances away from the central areas of carbonate accumulation. The Paskenta lens (~10 m long, Fig. 4A) and the Cold Fork lens (~260 m long) were sampled along their lengths, whereas the Wilbur Springs deposits were quarried previously, and hence only broken float blocks could be sampled (Campbell 1995).

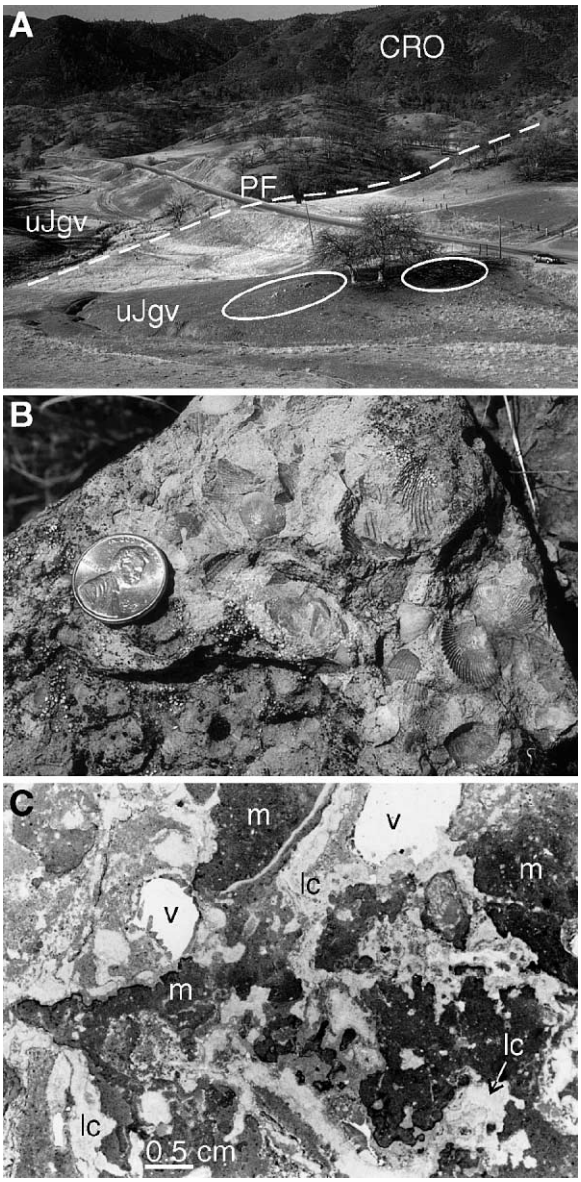

Fig. 4. Typical outcrop, hand sample and broad petrographic characteristics of Mesozoic seep-carbonates, California. (A) Paskenta field locality, situated between Digger Creek (left and foreground) and county road A9; view to west. Illustrated geology includes: isolated seep-carbonate mounds (circles) enclosed by fine-grained slope turbidites of Upper Jurassic Great Valley Group (uJgv), synsedimentary Paskenta Fault zone (broken line, PF) and tectonically juxtaposed Coast Range Ophiolite (CRO). (B) Outcrop float block from Wilbur Springs seep-carbonate deposit, characterized by fossil-rich micrite and seep-restricted brachiopod *Peregrinella whitneyi* (cf. Campbell & Bottjer 1995b). Coin = 1.8 cm in diameter. (C) Entire thin section view (4.0 cm long, PS1-1A) of typical seep-carbonate, broadly divisible into dark micrite (m) and light-coloured cements (lc), separated by dark, irregular, pyrite-coated corrosion surfaces. Clear calcite spar-filled vugs (v) common. Transmitted light.

RESULTS OF LABORATORY STUDIES

A detailed petrographic, stable isotopic and elemental analysis of carbonates collected from the three study sites led to the recognition of a recurring cement stratigraphy, and an inferred fluid-diagenetic history that was broadly similar among localities. Hence, this relative temporal framework allowed the elucidation of the evolving geochemical conditions that influenced the nature and timing of seep organism activity and palaeoenvironmental change. Laboratory results are outlined in the following sections, followed by the interpretation and discussion of these petrographic, isotopic and compositional data.

Petrography and paragenesis of three Californian Mesozoic seep deposits

Overview

A recurring paragenetic sequence was identified for the three study sites, including four major carbonate phases, one common sulphide phase, 10 minor phases (various carbonate or sulphate precipitates, internal siliciclastics) and three corrosion events (CE1–CE3) (carbonate phases outlined in Table 1). Corrosion was either accompanied by an iron-rich mineral phase (pyrite coating, CE1), or was nonferroan (CE2, CE3). The relative timing for all 18 paragenetic phases/events is summarized schematically in Fig. 5. Volumetrically speaking, only five distinct mineralogical and textural phases dominated the Californian seep deposits (see asterisks in Fig. 5; Figs 6 and 7A). A similar paragenetic sequence was reported from Cretaceous methane seep-carbonates of the Canadian Arctic (Beauchamp *et al.* 1989; Beauchamp & Savard 1992; Savard *et al.* 1996). For the Californian sites, the complete sequence of paragenetic events (Fig. 5) may be grouped into two main diagenetic stages: (i) early seafloor (events 1–7; Fig. 7) with concurrent organism activity; and (2) pore-associated, late burial-diagenetic (events 8–18; Fig. 8), with no preserved biotic associations. In addition, the taphonomy and petrography of fossil worm tubes (Fig. 9) are evaluated below. These structures were important in acting as open conduits for fluid migration, especially during later burial diagenesis, long after the primary seep plumbing had been occluded by cementation. Thus, the presence of tube worm animals early in seep history strongly influenced the later fluid-diagenetic record that was preserved in the Californian seep deposits. Finally, with respect to cement stratigraphy, we summarize the character and relative paragenetic position of probable microbial textures (Fig. 10).

Early diagenetic stage

The earliest events of paragenesis occurred in conjunction with colonization by a mega-invertebrate benthos; hence, early fluid seepage is inferred to have occurred at or near the sediment–water interface. In particular, most seep fossils were associated with the earliest micrite phase (micrite 1, event 1, e.g. Figs 4B,C and 7B), which preserved abundant, whole to fragmented mega-fossils, calcispheres, radiolaria, foraminifera, ostracodes and bioturbation structures. Micrite 1 also contained disseminated pyrite and abundant silt–sand-sized detritus from the host turbidites. Pervasive corrosion (CE1), coeval with and post-dating the micrite, created vugs and irregular surfaces which, in places, were lined with pyrite precipitates (event 2; Fig. 4C). Following corrosion, remnant micritic peloids and pyrite-encrusted micrite islands commonly were all that remained of the early micrite phase; subsequently, residual micrite regions were engulfed by younger cements (Figs 4C, 6 and 7A).

Worm tubes (event 3) and other surfaces were subsequently coated by a distinctive carbonate phase (event 4) that appears in thin section as an anhedral yellow calcite cement (cf. Beauchamp & Savard 1992). This ubiquitous cement typically contained inclusions of organic matter and pyrite, and either filled spaces or encrusted existing grains (Figs 6 and 7A). The yellow calcite likely formed as an aggrading, *in situ* replacement of the early micrite, probably related to dissolution associated with CE1, as indicated by the emergence and growth of yellow calcite crystals from corroded micrite 1 regions. Both carbonate phases displayed similar brightness patterns under CL (orange to bright orange). A carbonate phase that occurs both as primary cement and as neomorphic replacement spar has been documented in other geological settings (e.g. Fouke 1994).

The next major early cement phase consisted of a pervasive fibrous cement (fibrous 1 cement), which formed botryoids or radiating isopachous horizons (event 5) that typically grade outward from, or are interlayered with, the yellow calcite described above (Figs 6 and 7A). Fan-like subcrystals of fibrous cement displayed undulose extinction in cross-polarized light, and were nonluminescent under CL. At the Paskenta locality, fibrous cements encased dark inclusions that appeared as reddish to yellow–brown globules or black streaks in plane-polarized light (Fig. 7C–E). The dark inclusions fluoresced bright yellow-green under UV (Fig. 7D), and are inferred to be entrapped hydrocarbons. Fibrous cements from the Cold Fork and Wilbur Springs sites do not contain these inclusions, either because of diagenetic modification, or liquid hydrocarbons may not have been entrained in the fluids from these localities. A final, unique characteristic of the fibrous cement is an inferred boring structure of a marine organism (Fig. 7E), which was most clearly revealed under CL (Fig. 7F). The presence of the boring (event 6), which cut through both micrite and fibrous cement, indicates that a hard ground existed on the seafloor prior to burial.

Geopetal fillings or linings of micrite (micrite 2, detrital-poor, ±peloids) (event 7) were most common at the transition between early and late diagenetic stages (Figs 5 and 6).

Table 1 Petrographic characteristics of carbonate phases from the three Mesozoic hydrocarbon seep deposits of this study; also shown are figure numbers in the text for illustrations of each phase.

Paragenetic carbonate phase	Petrographic character	Crystal morphology	Crystal size	Cathodoluminescent (CL) character	Occurrence	Figure
Micrite 1 (m1)	Brown/grey, microcrystalline; quartz, feldspar detritus; pyrite, iron oxide, organics; ± fossil metazoa, peloids, bioturbation, intraclasts, microspar, fenestral (d, sp3), structure grumeleuse	Anhedral	Micrite <4 μm; microspar mosaics 5–15 μm	Homogeneous to mottled; dull to moderately bright orange	P, C, W	4B, C, 6, 7A, B, E, F, 8A, B, G, H, 9, 10
Yellow calcite (y)	Dark yellow, with entrained organics, pyrite grains; as cements (coatings, layers), or as irregular, aggraded regions engulfing m1; fenestral (sp3)	Anhedral	Variable thickness; on worm tubes, to ~100 μm	Homogeneous (cement) to mottled (replacive); dull to moderately bright orange	P, C, W	4C, 6, 7A, C, D, 9, 10D
Fibrous 1 calcite (f1)	Light grey/buff; radiating crystallite fans and undulose extinction, rhomb-tip terminations; clear regions with thin, turbid, inclusion-rich bands; as layers, growth cements in pores; ± borings, oil inclusions	Radial fibrous; radiaxial fibrous, with adjacent or alternating pyramidal or tabular habits	To 5 mm thick horizons, also in botryoidal splays	Homogeneous, dark; ± concentric zonations (cz): in large crystals — faint, dark, irregularly alternating thick–thin bands; in small pores — thin, sharp, jagged, brighter bands	P, C, W	4C, 6, 7A, C–F, 8C–H, 9
Dentate calcite (d)	Clear; as transparent regions in pore centres where several f1 tips meets; or as stellate cement in worm tubes and calcispheres	Inwardly stellate, subhedral rhombs and crystals	To 100 μm	Homogeneous to zoned: either dark to nonluminescent, or thin dark–bright alternations in cz	P, C, W	8A, B, 10D
Micrite 2 (m2)	Dark brown/grey; as fill (± clear calcite spar, peloids); or as thin, nondetrital cement clots, coatings, linings (?microbial); ± fractures	Anhedral	<4 μm	Mottled; moderately bright orange luminescence	P, C, W	6, 9F, 10
Isopachous calcite (i)	Whitish grey to`grainy' translucent; inclusion-rich; as thin layers lining pores	Anhedral	To 100 μm	Mottled; dull to bright orange	P, C, W	8A–D
Rhombohedral calcite (rh)	Demarcated rhombs in CL, not visible in transmitted light; as growth cement in pores	Euhedral rhombs	To 100 μm	Homogeneous; dull orange; fuzzy-thick to sharp-thin cz	C, W	8C, D
Calcite spar 1 (sp1)	Clear, blocky; as pore filling cement	Subhedral to euhedral	To 1.5 cm thick	Homogeneous to faintly mottled; dark orange	C, W	8E, F

Table 1 continued

Paragenetic carbonate phase	Petrographic character	Crystal morphology	Crystal size	Cathodoluminescent (CL) character	Occurrence	Figure
Calcite spar 2 (sp2)	Clear, blocky, with well-developed cleavage striae, as pore-filling cement	Euhedral	To 1.5 cm thick	Homogeneous, moderately bright orange; ± thin to thick sectoral zonation with orange/yellow regions	P, C, W	4C, 6, 8A–D, 9F, 10C
Calcite spar 3 (sp3)	Clear, with irregular, embayed margins; occurs at phase boundaries, along fractures, filling fenestrae (m1, y)	?Anhedral	Several mm thick	Homogeneous; bright yellow to orange	P, C, W	6, 8G, H
Fibrous 2 calcite (f2)	As concentric bands within f1; some bands connect at phase boundaries to sp3 fenestrae	Mimics radial fibrous habit of original crystal	To 150 μm thick	Homogeneous; bright yellow orange; ± thin, faint cz	P, W	9G, H

In places, this pore-associated, nondetrital micrite disrupted or was intercalated with the fibrous cements discussed above.

Late diagenetic stage

The paragenetic phases and events of late diagenesis were recorded in pores and voids, or by late-stage dissolution/recrystallization of selected fabrics (Fig. 8). The onset of late diagenesis was marked by nonferroan corrosion (CE2, event 8) along vug margins (e.g. Fig. 6), and the formation of several rim cement types. For example, a nonluminescent, interlocking, dentate cement (event 9) rimmed some cavities (Fig. 8A,B), and engulfed acicular splays of remnant aragonite in some fibrous cements, both of which displayed the same dark CL pattern (Fig. 8B). Another rim fabric type consisted of thin horizons (~100 μm thick) of an inclusion-rich, isopachous calcite (event 10; Fig. 8A–D), which was associated with cavity margins, or the outermost tips of some fibrous cements. These isopachous rims exhibited a grainy to mottled, dull to bright orange luminescence, which is suggestive of recrystallization, probably from the earlier formed fibrous 1 or dentate cements that were spatially affiliated with this later, inclusion-rich phase.

Remaining porosity was filled by late-stage carbonate, siliciclastic and sulphate phases (events 11–14; Fig. 5). In places (e.g. Fig. 8C,D), the inclusion-rich isopachous crusts were overlain by rhombohedral calcite (event 11). Many pores were filled or lined with a detrital silt–clay (event 12), which appeared golden-yellow in hand samples (Fig. 9A,B), or golden-brown to dark-brown in thin section (e.g. Figs 4C and 8C,D). This phase commonly contained variable amounts of angular quartz and feldspar grains, and preceded or was concurrent with the precipitation of late blocky calcite (calcite spars 1, 2, events 13, 15; Fig. 5) and barite (event 14). Calcite spars 1 and 2 were differentiated by dark-orange and orange CL, respectively; spar luminescence appeared homogeneous or mottled, or showed sectoral zonation (e.g. Fig. 8B,D,F). Barite occurred as fine admixtures with the silt–clay fill, or as distinct, strongly birefringent, prismatic crystals (Fig. 8E,F), which were wedged among blocky calcite spar crystals.

The youngest fracture–dissolution–recrystallization event (CE3, event 16) was fabric selective, and created mouldic porosity, particularly within anhedral yellow calcite (e.g. Figs 6 and 7A,C). In addition, CE3 was associated with irregular recrystallization bands within the early fibrous 1 cement that formed a distinctive late-stage feature (fibrous cement 2, event 17; Fig. 5), not conspicuous in plane-polarized light (Fig. 8G). However, the recrystallized fibrous 2 cement was easily distinguished by its bright yellow–orange luminescence, where it cut across unaltered, nonluminescent, early fibrous cement (Fig. 8H). Commonly, the recrystallized bands of the late fibrous cement were spatially connected to scattered, small dissolution fenestrae filled with the ultimate

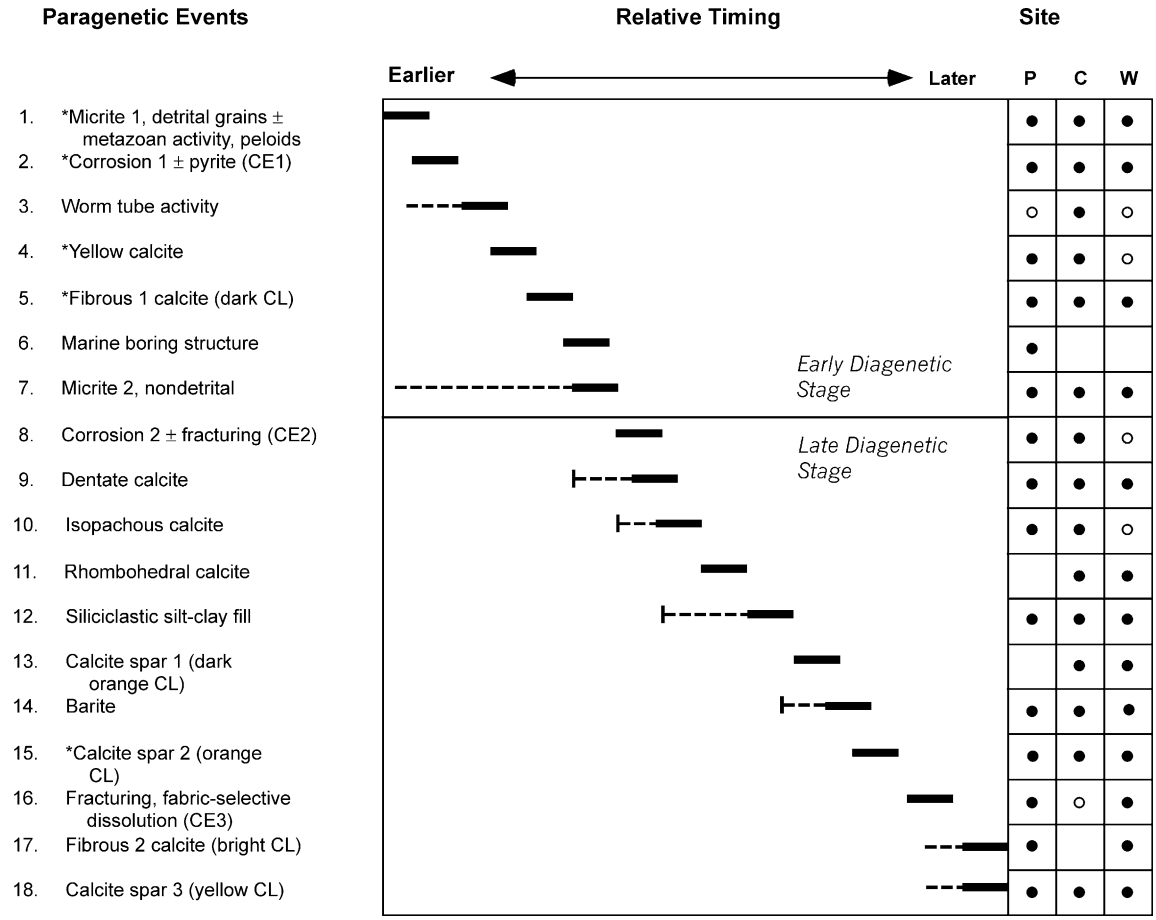

Fig. 5. Relative timing relationships and distributions of the 18 paragenetic events recorded in the three Mesozoic seep-carbonate deposits of this study, western California. Division between early and late diagenetic stages is shown. Corrosion events labelled as CE1, CE2, CE3. Full lines indicate relative duration and timing; broken lines suggest probable maximum extent of event. Asterisks indicate major phases or events. Distribution of events across the three sites (Paskenta, P; Cold Fork of Cottonwood Creek, C; Wilbur Springs, W) shown on right, with filled circles indicating major occurrence and open circles representing minor occurrence of an event or phase at a given site.

diagenetic phase, clear calcite spar 3 (event 18; Figs 5 and 8G). This calcite spar characteristically luminesced yellow–orange (Fig. 8H), typical of cements formed from late burial fluids.

Taphonomy and petrography of worm tubes

Fossil worm tubes (Fig. 9), where present, are significant for two reasons. First, they indicate that these organisms colonized the Californian seep system somewhat later in the paragenetic sequence (event 4, with yellow calcite) than most seep mega-fossils (event 1, with micrite 1). Second, many later diagenetic phases of the paragenetic sequence filled the internal spaces of the fossil worm tubes. At modern hydrothermal vents, entombed tube worms have been shown to remain open to fluid flow long after occlusion of primary porosity during progressive mineralization of the vent plumbing (cf. Cook & Stakes 1995). Therefore, in any given seep deposit, precipitates that formed around and within worm tubes are likely to have captured a significantly greater proportion of the fluid-diagenetic history.

In the Californian Mesozoic seep-carbonates, worm tubes occurred both as large structures (2–5 mm width, to at least 15 cm length; Fig. 9A–C,F), and as small clusters of tubes (0.2–0.5 mm width of individual tubes; Fig. 9A–C,E). These tube diameters are consistent with the reported size ranges of some diminutive modern vestimentiferans (e.g. Southward 1991). Larger tube structures preserved multiple generations of cementation and siliciclastic fill (Figs 8C,D and 9A–C,F). The circular tube cross-sections generally were demarcated by thin rims of yellow calcite cement, which appeared in hand samples as sharp, dark grey delineations (Fig. 9A,B), and in thin section as ~100-μm-thick yellow coatings (Fig. 9C,E,F). In many instances, this encrusting yellow cement permineralized and mineralogically replaced the outer walls of tubes while the worms were alive, as indicated by the uniform and distinct preservation of tube cross-sections, with little

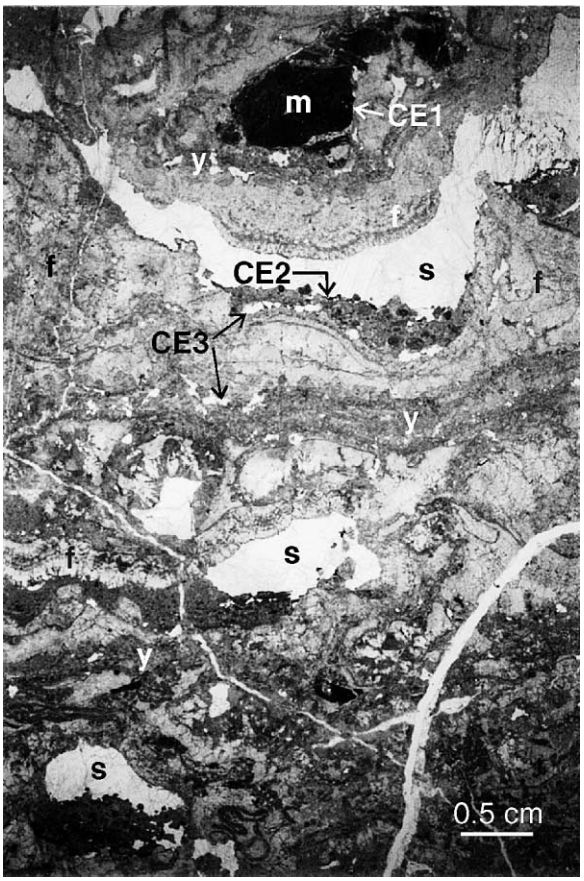

Fig. 6. Entire thin section view (4.0 cm long, PN1-9A) illustrating the four major carbonate cement phases (asterisks in Fig. 5): micrite 1 (m), anhedral yellow calcite (y), fibrous 1 calcite (f) and blocky spar 2 (s). The three corrosion events are indicated by CE1, CE2, CE3. Large vugs (white) formed during CE1; their geopetal fill is recrystallized peloidal micrite (micrite 2). Transmitted light.

evidence for the decay or collapse of walls prior to cementing. In rare examples (Fig. 9E), original tube walls were preserved as thin, brown residues encased by yellow calcite cement rims. However, more commonly the walls decayed away after encrustation, leaving only the yellow calcite to preserve the tube. Original tube walls probably were constructed of an organic, proteinaceous and chitinous material (cf. Shillito *et al.* 1995). Internal septae are visible in some larger specimens (Fig. 9C), and some worm tubes were coated with framboidal pyrite (Fig. 9C). In reflected light (Fig. 9D), the pyrite exhibited oxidation rinds, which were illuminated as thin, darker rims around unaltered (white) pyritic interiors. Once the animals died, both exterior and interior tube surfaces were coated and infilled by phases that post-dated the pyrite and yellow calcite (Figs 8C,D and 9).

Microbial sedimentary textures

Some nondetrital micrite (micrite 2) occurred in unusual textural and spatial relationships with respect to the early diagenetic phases at all three Californian Mesozoic seep localities (Fig. 10). These relationships included: (i) finely laminated micrite, which coated corrosion horizons (e.g. Fig. 10A,B), or lined pores and cavities (e.g. Fig. 10C); (ii) micritic peloids with indistinct margins, surrounded by translucent microspar (e.g. matrix of Figs 9C,E and 10D); and (iii) clotted micrite clumps draped from the interior walls of worm tubes (e.g. Fig. 9E), or encrusting worm tube surfaces (e.g. Fig. 10D). The Californian examples are texturally similar to putative microbial fabrics identified in Italian seep-carbonates of Miocene age (cf. Cavagna *et al.* 1999, Fig. 6a,b, p. 263, and Figs 9 and 10, p. 266–267; Clari & Martire 2000). A molecular biomarker analysis of the Italian material confirmed the microbial origin of these distinctive textures (Peckmann *et al.* 1999a; Thiel *et al.* 1999). The inferred microbial fabrics of the Californian Mesozoic seep-carbonates occurred throughout the early, preburial stage, and are under further study.

Stable isotopes of carbonate carbon and oxygen

The results of stable isotopic analysis of the carbonates of the three Californian deposits (Table 2, Fig. 11) indicate a methane-derived origin. This inference is based on the observed depletion in carbonate ^{13}C (cf. Aharon 2000; Kauffman *et al.* 1996; Ritger *et al.* 1987; Suess & Whiticar 1989) of as low as −43.8‰ Pee Dee Belemnite (PDB). In addition, individual carbonate phases formed discrete isotopic groups, and seep-carbonates could also be discriminated by locality. Material analyzed included major carbonate phases (e.g. micrite 1, yellow calcite, fibrous 1 cement, blocky calcite spar), shell-carbonate samples from early micrite phases and a concretion from nearby Paskenta turbidites (Table 2). Minor carbonate cement phases were not sampled because the spatial resolution of the drill was insufficient to avoid contamination of powders by adjacent phases.

A carbon versus oxygen isotopic cross-plot (Fig. 11) revealed a grouping of the data into four distinct fields, comprising the authigenic carbonates from each of the three localities and the shell-carbonate. Paskenta carbonate carbon was consistently the most ^{13}C depleted across all cement phases measured, with $\delta^{13}C$ values of approximately −27 to −44‰ PDB. Possible carbon sources for this range of depleted values include thermogenically sourced methane, mixed sources (thermogenic or biogenic methane + dissolved inorganic carbon (DIC) in seawater) or oil fractions (cf. Aharon *et al.* 1997). In comparison, the Cold Fork and Wilbur Springs carbonate carbon values were more similar to each other ($\delta^{13}C$ range of approximately −19 to −25‰ PDB), and suggest mixing of hydrocarbon and seawater DIC signatures (cf. Haggerty 1991) during formation. Shell-carbonate signatures all clustered in a separate field, near 0‰ PDB for both $\delta^{13}C$ and $\delta^{18}O$. This pattern is consistent with shell secretion near isotopic equilibrium with seawater bicarbonate (Anderson & Arthur 1983). Specifically,

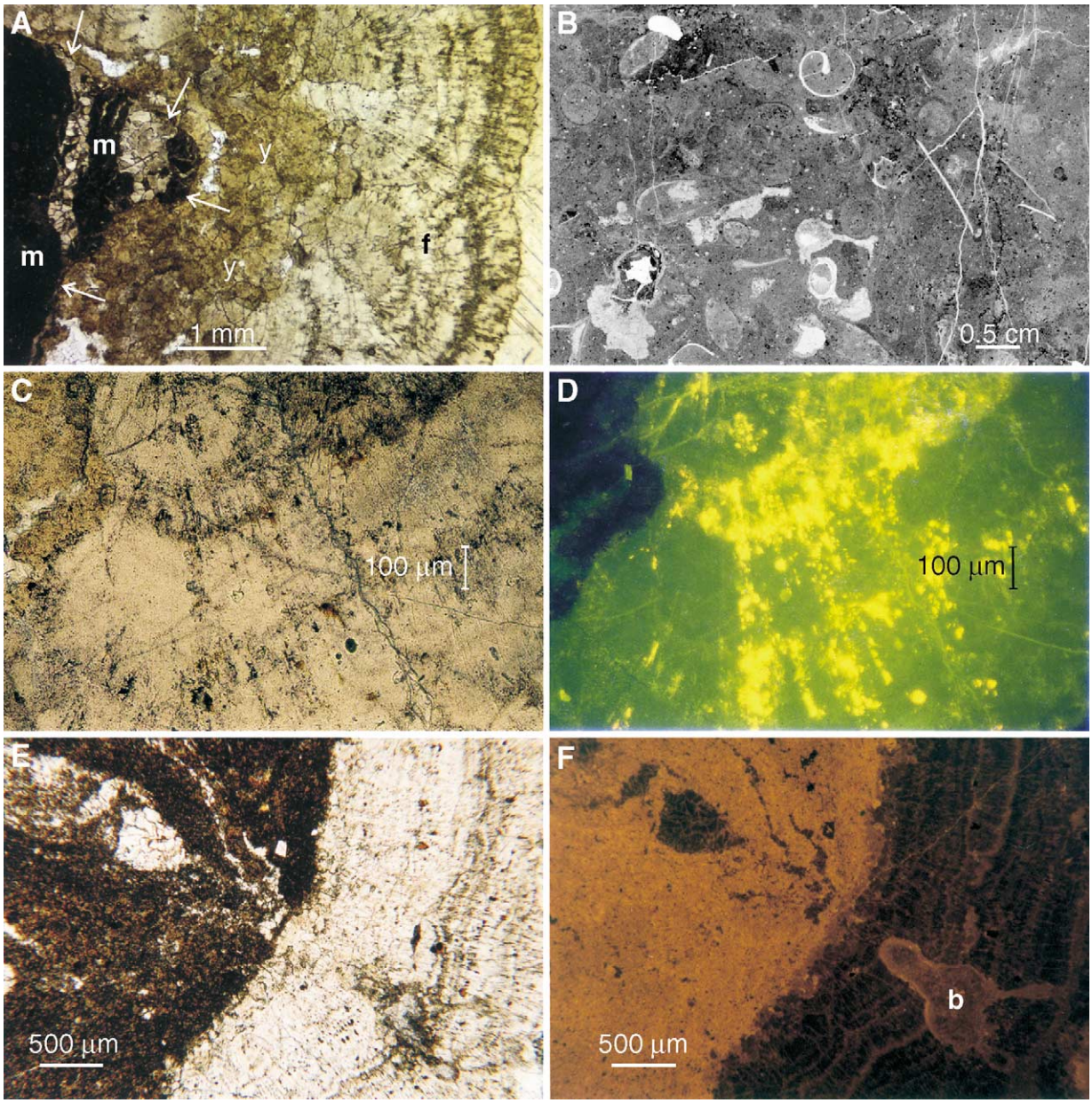

Fig. 7. Petrographic aspects of early events of cement stratigraphy. (A) Early diagenetic sequence (PN1-9A), from micrite 1 (m), to first corrosion event (CE1, arrows), to anhedral yellow calcite (y), to fibrous 1 cement (f). Plane-polarized light. (B) Bioturbated, detrital-rich micrite 1 phase, with gastropods, calcispheres and scattered pyrite grains. Entire thin section view (4.0 cm long, PS1-4A), transmitted light. (C) Transition from anhedral yellow calcite (upper left corner) to fibrous 1 cement, the latter exhibiting brown globules and black streaks inferred as petroleum inclusions (PN1-9A). Plane-polarized light. (D) Same view and magnification as in (C), in UV; hydrocarbon inclusions in the fibrous cement fluoresced bright yellow–green. (E) Micrite 1 overlain by fibrous 1 cement with golden to reddish brown petroleum inclusions (PN1-1D). Plane-polarized light. (F) Same view and magnification as in (E) in CL; marine boring structure (b, ~1.3 mm long) revealed in lower right corner.

shell-carbonate carbon values of $\delta^{13}C$ −2.4 to +2.2‰ PDB for Mesozoic Californian examples fell within the range reported by Rio *et al.* (1992) for modern seep shell-carbonate. Minor carbon isotopic depletion or enhancement of modern vent-bivalve shell-carbonate (to $\delta^{13}C$ ±3.5‰ PDB) has been attributed to chemosymbiotic life habits (e.g. Rio *et al.* 1992). Finally, a micritic concretion from fine-grained turbidites, ~100 m north-east of the Paskenta carbonate outcrop, yielded a comparatively elevated $\delta^{13}C$ signal of −4.3‰ PDB (Fig. 11). Such concretions are relatively common in Great Valley turbidites and typically contain normal marine fossils. Possible carbonate carbon origins include dissolution of shell-carbonate, mixing of seawater DIC with products of sedimentary organic decay or other sources.

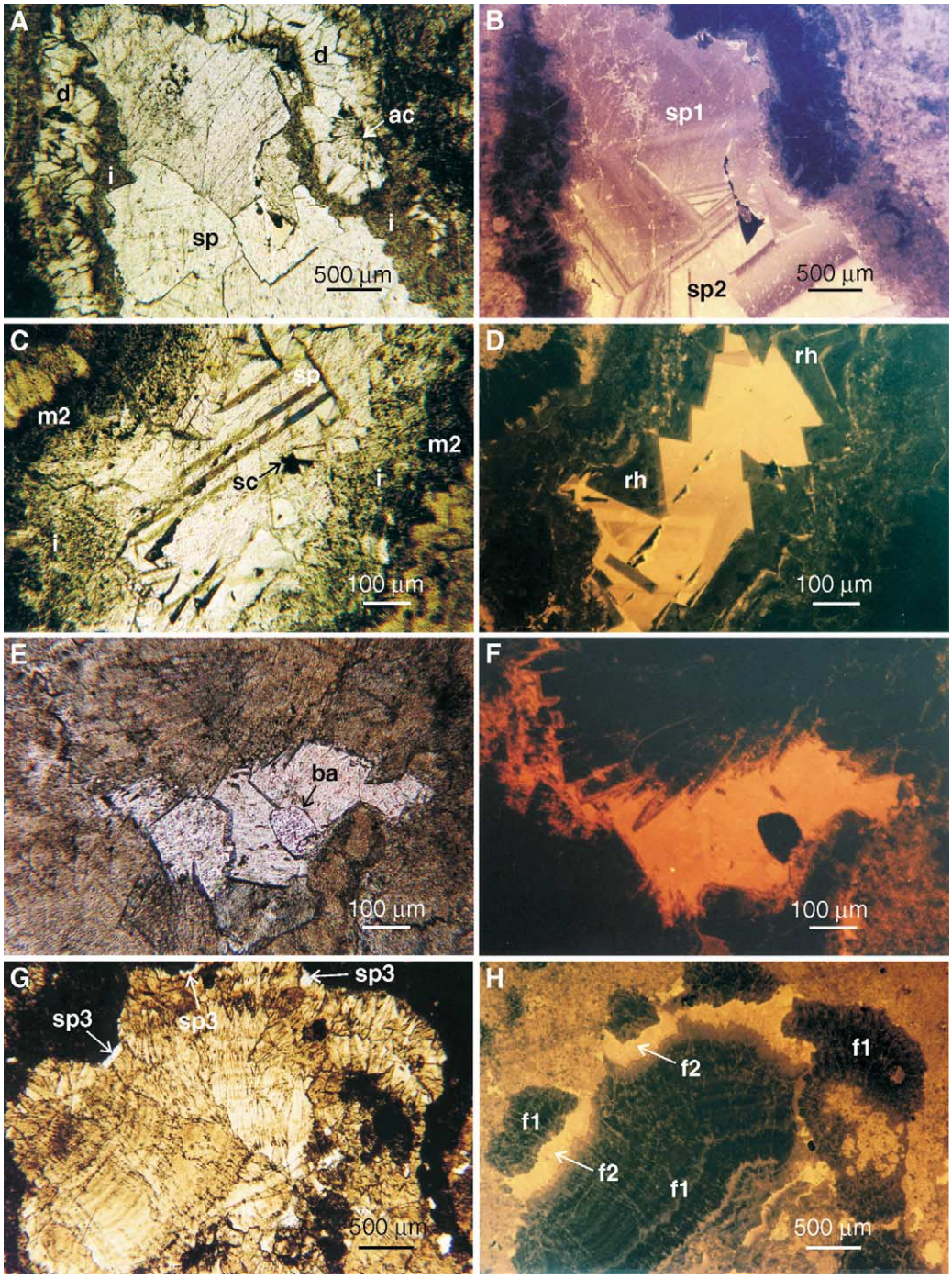

Fig. 8. Petrographic aspects of late diagenetic phases. (A) Cavity lined with dentate cement (d), inclusion-rich isopachous cement (i) and blocky calcite spar (sp.); dentate cement enclosed remnant acicular fibrous crystals (ac). CC-240-1, plane-polarized light. (B) Same view and magnification as in (A), in CL, displaying nonluminescent character of dentate and acicular fibrous cements, grainy dull orange CL of isopachous horizons and sectoral zonation of calcite spar – both dark orange (spar 1, sp1) and orange (spar 2, sp2) varieties. (C) Late-stage phases filling pore space in worm tube (CC-240-1), including micrite 2 lining (m2), inclusion-rich isopachous crust (i), blocky calcite spar (sp) and minor silt-clay (sc). Plane-polarized light. (D) Same view as in (C), in CL, revealing rhombohedral calcite (rh) phase not detected in transmitted light, and sectoral zoning of blocky calcite spar. (E) Details of radially fibrous cement and small pore cemented with late, blocky calcite spar and birefringent, prismatic barite crystal (ba). CC-80-5, plane-polarized light. (F) Same view and magnification as in (E), in CL, illuminating fibrous 1 subcrystal tips with laterally adjacent pyramidal and tabular habits, and nonluminescent character of barite. (G) Vug formed in micrite 1, filled with radially fibrous cement; minor moldic porosity (CE3) filled with late spar 3 (sp3). PN1-1A, plane-polarized light. (H) Same view and magnification as in (G), in CL, displaying darkly luminescent, early fibrous cement (f1) cut by band of bright yellow, recrystallized fibrous cement (f2); bright band spatially associated with fenestrae of late spar 3.

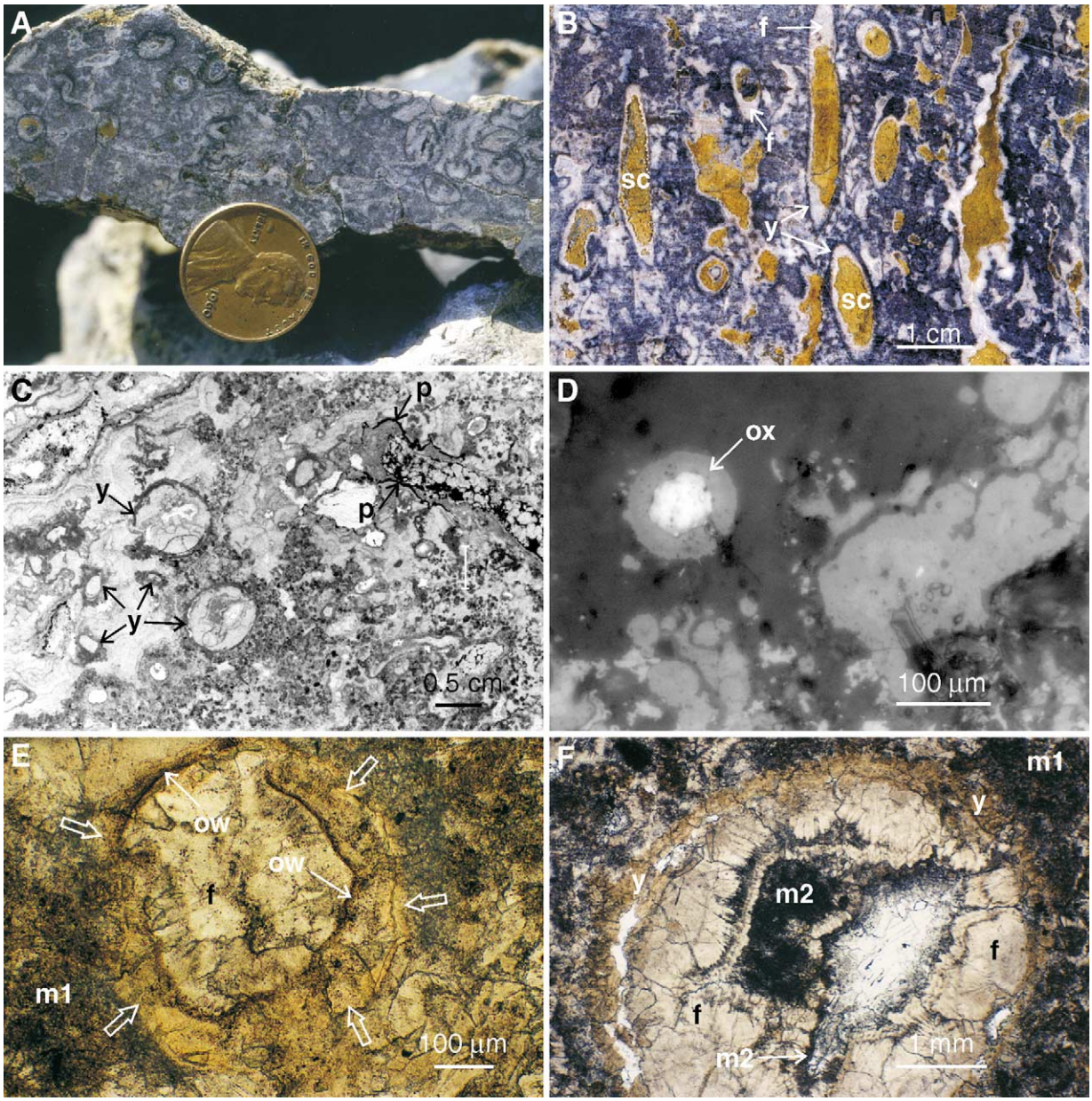

Fig. 9. Petrography and paragenetic associations of fossil worm tube structures, Cold Fork of Cottonwood Creek locality. (A) Hand sample of worm tube fabric in cross-section; both large (to 5 mm) and small (to 0.5 mm) tubes defined by thin, dark outlines. Coin = 1.8 cm in diameter. (B) Sawn slab surface of worm tube fossils in longitudinal and cross-section, and cemented vugs. Tubes delineated by dark outline (anhedral yellow calcite, y) and lined by fibrous cement (white, f), followed by fill of golden-yellow silt–clay (sc). (C) Entire thin section view (4.0 cm long, CC-240-1) of large- and small-diameter worm tube fossils in longitudinal and cross-section, surrounded by matrix of peloidal micrite and fibrous calcite. Tubes lined with thin rim of anhedral yellow calcite (y) or pyrite (p). Transmitted light. (D) Detail of pyrite-lined tube of (C) in reflected light, illustrating pyrite framboids (light coloured). One framboid illustrates well-preserved brassy yellow interior (white), with nonreflective, oxidized rim replacement (ox). (E) Small-diameter worm tube cross-section in micrite, showing thin, red–brown, organic tube wall (ow) that was encrusted by an ~70–100-µm-thick coating of anhedral yellow calcite (arrows), and later filled by fibrous cement (f). CC-60-3, plane-polarized light. (F) Detail of large-diameter worm tube from (C) in cross-section, in peloidal micrite 1, showing tube wall rim encrusted by anhedral yellow calcite (y) with late, mouldic porosity. Tube filled by successive, post-worm cement phases, including fibrous (f), clotted or lined micrite 2 (m2) and late spar (white centre). CC-240-1, plane-polarized light.

Oxygen isotopic signatures of carbonate phases from each of the three localities overlapped broadly, ranging from $\delta^{18}O$ −13.9‰ PDB (late blocky spar, Paskenta) to +2.3‰ PDB (fibrous calcite, Wilbur Springs) (Table 2). In general, fibrous cements from each of the three sites were the most enriched in ^{18}O for a given locality, and late blocky spars exhibited the most negative $\delta^{18}O$ values (Fig. 11). An exception was the Wilbur Springs deposit, which contained late blocky spars of variable oxygen isotopic signatures. Individual cement phases for each locality were separated into distinct $\delta^{18}O$

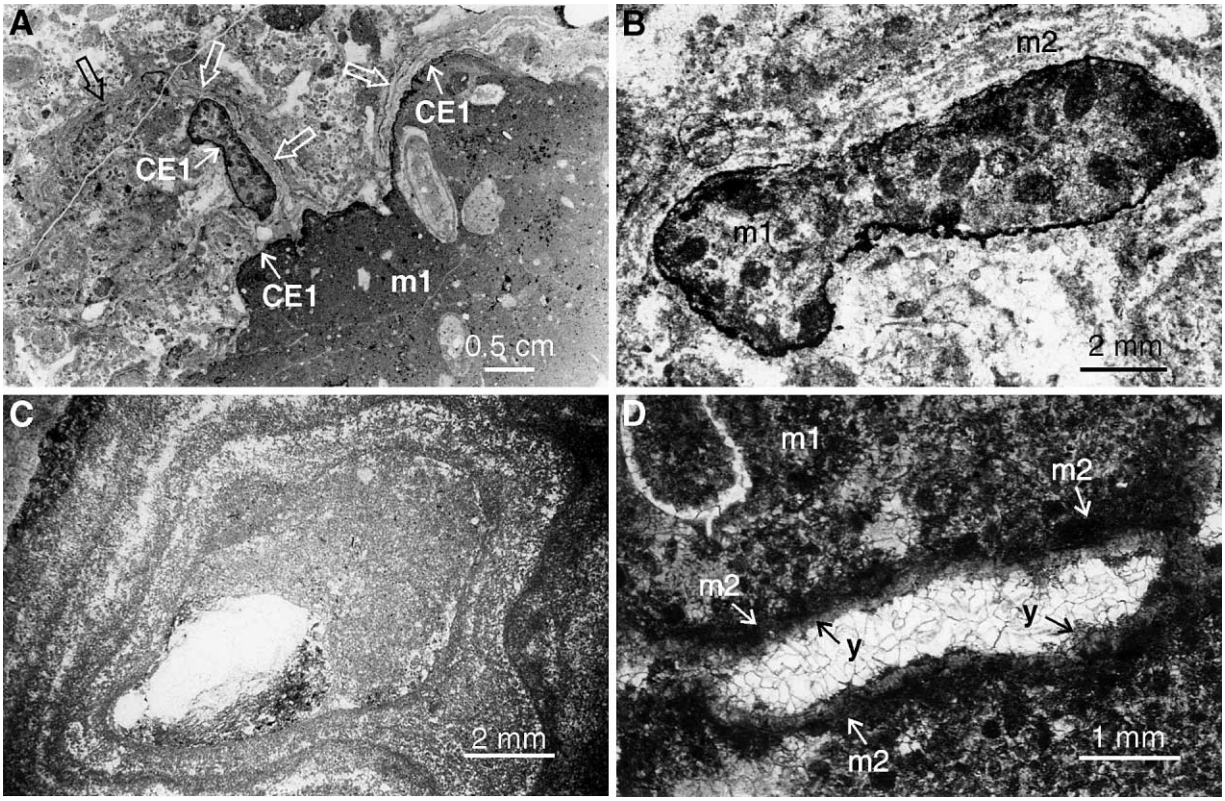

Fig. 10. Occurrences of probable microbial textures. (A) Entire thin section view (PS1-8A; 4.0 cm long) of remnant early micrite (m1), with corroded, pyrite-encrusted horizon (CE1) immediately overlain by thinly laminated micrite of probable microbial origin (arrows). Transmitted light. (B) Details of (A) showing peloid-rich, early micrite island remnant (m1) coated with framboidal pyrite, and subsequently encrusted by thinly laminated micrite (m2). Plane-polarized light. (C) Pore lined with finely clotted micrite laminae. WS-6, plane-polarized light. (D) Small worm tube in longitudinal section, surrounded by peloidal micrite (m1). Tube coated with anhedral yellow calcite (y) and clotted microbial micrite (m2), and filled with dentate cement (white). Gastropod in upper left. CC-60-3, plane-polarized light.

fields by cement type, except for those from the Wilbur Springs locality, which displayed generally clumped and relatively elevated $\delta^{18}O$ values across most phases (Fig. 11).

With respect to cement paragenesis, stable isotopic values follow a clear trend for some localities, best illustrated by the largest data set from Paskenta. Figure 12 depicts average $\delta^{18}O$ versus $\delta^{13}C$ values for major Paskenta seep-carbonate phases, with arrows tracing relative order in the cement stratigraphy. At the onset of hydrocarbon seepage, Paskenta micrites were moderately depleted in both ^{13}C and ^{18}O content. From this starting point, further depletion in ^{13}C but enrichment in ^{18}O is evident through the remaining early sequence of yellow to fibrous calcite phases (Fig. 12). Elevated $\delta^{18}O$ values of fibrous cements are consistent with their precipitation in contact with cold, oxidizing seawater (Anderson & Arthur 1983). Isotopic values follow a reverse trend in the late diagenetic stage, with post-fibrous phases (isopachous, blocky spar) exhibiting elevated $\delta^{13}C$ and increazingly negative $\delta^{18}O$ signatures, consistent with fluids that were possibly meteoric influenced, warm (to 100°C) or of unusual, late burial composition (cf. Land 1989). A similar oxygen isotopic pattern is suggested by the spread of Cold Fork cement phases with respect to $\delta^{18}O$ (Fig. 11); however, fewer measurements from these seep-carbonates precluded a detailed assessment of possible trends. Wilbur Springs oxygen isotopic values were irregularly scattered with respect to cement phase (Fig. 11).

Compared to Paskenta and Cold Fork of Cottonwood Creek deposits, Wilbur Springs carbonates were more elevated in $\delta^{18}O$, but yielded more scattered isotopic signatures with respect to cement stratigraphy (Fig. 11). Seafloor serpentinite–seawater interactions associated with diapiric intrusion and submarine mobilization may have influenced Wilbur Springs isotopic signals. For example, elsewhere in the area, acicular aragonite directly cemented seafloor serpentinite–breccia piles (Carlson 1984b). This phenomenon suggests that normal seawater mixed with fluids leaking from the serpentinite that were ultimately derived from dewatering of the subjacent oceanic plate (Coast Range Ophiolite). Carbonate $\delta^{18}O$ signatures (+2 to +8‰ PDB) from modern analogous Marianas seep-carbonates that formed above serpentine diapirs were interpreted to represent cold formation waters

Table 2 Stable carbon and oxygen isotope values for dominant carbonate components from Paskenta, Cold Fork of Cottonwood Creek and Wilbur Springs localities.

Sample number	Carbonate phase	$\delta^{13}C‰$ (PDB)*	$\delta^{18}O‰$ (PDB)*
Paskenta			
PC1 (*Cooperrhynchia*)	Brach iopod shell	−2.4	−0.6
PC2 (*Cooperrhynchia*)	Brach iopod shell	−0.7	−0.1
PB2 (*Buchia*)	Bivalve shell	+2.2	−0.9
PN1-1A-4	Micrite 1	−33.3	−10.5
PS1-3B-1	Micrite 1	−35.5	−10.2
PN1-2B-2	Micrite 1	−35.3	−10.8
PS1-1A-1	Micrite 1	−32.3	−10.8
PN2-3A-2	Micrite 1	−32.1	−7.8
PN1-9A-1	Yellow	−37.8	−9.8
PN1-9B-3	Yellow	−36.5	−8.0
PN1-7B-1	Yellow	−36.1	−7.3
PN1-9A-2	Yellow	−38.0	−7.4
PN1-11B-1	Yellow	−35.1	−8.2
PN1-13A-1	Yellow	−32.4	−6.5
PN2-2A-1	Yellow	−35.7	−7.4
PN1-12B-2	Fibrous 1 + yellow	−37.2	−5.5
PN1-9B-1	Fibrous 1	−40.1	−2.0
PN1-9A-3	Fibrous 1	−41.4	−0.7
PN1-11B-2	Fibrous 1	−34.4	−3.4
PN2-3A-3	Fibrous 1	−41.0	−0.9
PSK-1	Fibrous 1	−34.5	−3.9
PSK-3	Fibrous 1	−36.5	−3.3
PSK-4	Fibrous 1	−39.6	−0.5
PSK-5	Fibrous 1	−43.7	−1.2
PSK-6	Fibrous 1	−36.0	−3.8
PN1-5B-1	Isopachous	−36.2	−6.9
PN1-5A-1	Blocky spar	−38.4	−13.8
PN1-9B-2	Blocky spar	−27.9	−13.4
PN1-7B-2	Blocky spar	−37.2	−12.8
PN1-9A-4	Blocky spar	−37.5	−13.4
PN1-9A-5	Blocky spar	−33.3	−13.5
PN1-12B-1	Blocky spar	−29.0	−12.9
PT2-2-1	Concretion	-4.3	−13.9
Cold fork of cottonwood creek			
CC-60-4-2	Micrite 1	−24.9	−7.4
CC-80-5-1	Yellow	−20.6	−8.0
CC-80-4-1	Yellow	−21.4	−8.9
CC-80-5-2	Fibrous 1	−21.8	−5.1
CC-80-4-2	Fibrous 1	−20.1	−4.3
CC-20-1-2	Fibrous 1	−23.4	−3.0
CC-60-5-1	Blocky spar	−20.3	−11.3
Wilbur springs			
WS-16-2 (*Peregrinella*)	Brach iopod shell	+0.5	+0.7
WS-7-2	Micrite 1	−21.5	−0.5
WS-6-4	Micrite 1	−21.3	+0.9
WS-6-3i	Micrite 1	−22.1	+1.8
WS-6-3ii	Micrite 1	−22.2	+1.7
WS-2-1	Micrite 1	−19.3	+1.5
WS-7-1	Fibrous 1	−22.3	+2.2
WS-6-1	Fibrous 1	−23.9	+1.3
WS-7-3	Fibrous 1	−22.2	+2.0
WS-9-2	Fibrous 1	−21.7	+2.3
WS-14-1i	Fibrous 1	−24.3	+1.8
WS-14-1ii	Fibrous 1	−21.3	+1.1
WS-4-1	Blocky spar	−19.4	−5.2
WS-5-2	Blocky spar	−19.5	+0.8
WS-12-1	Blocky spar	−21.8	+2.2

Blocky spar, undifferentiated spar 1 and 2; i, ii, replicate samples.
*Uncertainty, ±0.1‰.

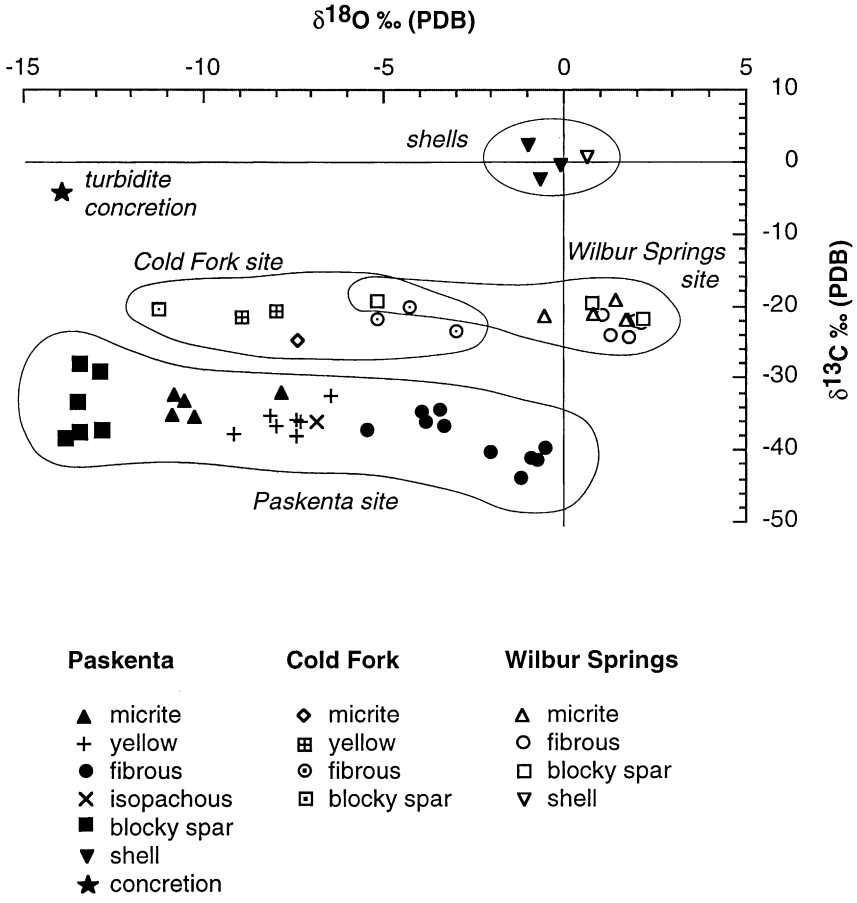

Fig. 11. Stable carbon versus oxygen isotopic cross-plot for Paskenta, Cold Fork of Cottonwood Creek and Wilbur Springs seep-carbonate deposits revealed four distinct fields (encircled).

(Haggerty 1991). In contrast, Wilbur Springs seep-carbonate phases exhibited lower $\delta^{18}O$ values (approximately −5 to +2‰ PDB), and may reflect somewhat warmer formation conditions. It is unlikely that meteoric waters infiltrated the Californian Mesozoic carbonates because shell values of well-preserved fossil specimens enclosed in the seep-micrites recorded isotopic signatures similar to seawater signals (Fig. 11).

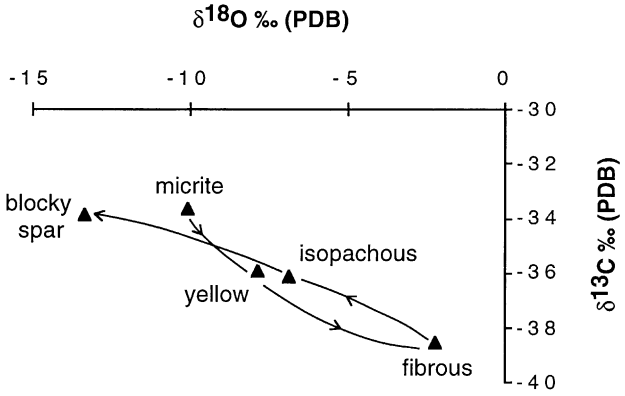

Fig. 12. Dominant carbonate phases from the Paskenta locality illustrate a stable isotopic trend with respect to cement stratigraphy. Arrows follow averaged $\delta^{18}O$ and $\delta^{13}C$ values for cement stratigraphy, from early to late carbonate phases.

Elemental distributions in carbonate phases

Individual carbonate phases of the Californian seep deposits were also analyzed for their major, minor and trace elemental compositions, in order to track the evolution of seep fluids and to assess the microchemical conditions experienced by the affiliated mega-invertebrates and chemosynthetic micro-organisms. The choice of measured elements for electron probe microanalysis (EPMA) was dictated by the reported geochemistry for typical, present-day, low-temperature hydrothermal vent and cold seep fluids and precipitates. Mean elemental values are shown in Table 3.

Similar to the results obtained for isotopic analysis, EPMA revealed distinctive groupings with respect to both carbonate phase and locality (Table 3). Early micrites (micrite 1) at all three localities contained relatively high Fe (~1500–6200 p.p.m.), moderate Mg, Sr and S, and variable Mn (~300–1350 p.p.m.) concentrations, compared to all other carbonate phases. A high detrital grain component in micrite 1 resulted in relatively high concentrations of Si, Al, K, Na

Table 3 Mean elemental composition data for major carbonate phases of the three Californian Mesozoic seep deposits of this study. Ca, Mg, Fe, Sr, Mn, Si, Al, K, Na, Ti, S and Ba contents (p.p.m.) shown for electron probe microanalysis (EPMA) spot analyses. Carbonate ion concentration (not shown) was calculated based on a one-to-one atom of Ca. High totals for early micrite 1 are attributed to sample inhomogeneity caused by particularly high detrital content for this phase.

Carbonate phase (# analyses)	Ca el % (p.p.m.)	Mg el% (p.p.m.)	mol% Mg	Fe el % (p.p.m.)	Sr el % (p.p.m.)	Mn el % (p.p.m.)	Si el % (p.p.m.)	Al el % (p.p.m.)	K el % (p.p.m.)	Na el % (p.p.m.)	Ti el % (p.p.m.)	S el % (p.p.m.)	Ba el % (p.p.m.)	Totals (%)
Detection limit (p.p.m.) (single line), 99%	–	90		40	60	40	20	10	20	30	50	20	170	
SD standard calcite UCB #135	1030	80		20	10	20	10	10	10	10	50	10	110	
Paskenta														
Micrite 1 (9)	361863	6689	2.8	2395	796	1346	19387	5076	1192	1384	219	138	b.d.	106.6
Anhedral yellow (8)	384902	5084	2.1	369	808	830	161	25	47	227	b.d.	102	b.d.	98.4
Fibrous 1 (dark CL) (18)	376455	13150	5.4	51	1084	58	275	24	49	776	b.d.	98	b.d.	99.1
Fibrous 2 (bright CL) (5)	376104	12212	5.0	b.d.	1109	662	455	20	36	485	b.d.	88	b.d.	98.9
Spar 2 (orange CL) (14)	386567	4391	1.8	438	729	690	96	19	47	b.d.	b.d.	b.d.	b.d.	98.4
Spar 3 (yellow CL) (7)	388858	259	0.1	498	1207	3212	72	12	38	b.d.	b.d.	b.d.	b.d.	98.2
Cold Fork of Cottonwood Creek														
Micrite 1 (16)	379203	4233	1.7	1577	482	605	9367	2578	573	306	179	193	b.d.	103.1
Micrite 2 (19)	381792	5238	2.2	1372	507	455	4298	1653	322	254	114	135	b.d.	100.8
Anhedral yellow (15)	385768	6008	2.5	391	602	480	254	35	37	216	b.d.	198	b.d.	99.0
Fibrous 1 (dark CL) (7)	381553	11951	4.9	b.d.	981	b.d.	421	13	23	479	b.d.	76	b.d.	99.9
Dentate calcite (6)	381233	10642	4.4	131	453	101	59	33	54	137	b.d.	60	b.d.	99.1
Isopachous calcite (4)	393839	4027	1.7	70	362	58	278	b.d.	b.d.	78	54	83	b.d.	100.0
Rhombohedral calcite (5)	396787	2198	0.9	148	544	64	98	b.d.	b.d.	b.d.	53	b.d.	b.d.	100.0
Spar 2 (orange CL) (6)	391497	249	0.1	453	485	1209	100	b.d.	b.d.	b.d.	b.d.	b.d.	b.d.	98.3
Spar 1 (dark orange CL) (7)	387828	2352	1.0	2819	293	916	3264	1218	261	62	78	37	b.d.	100.8
Spar 3 (yellow CL) (19)	390497	890	0.4	1286	328	1269	855	308	125	b.d.	b.d.	42	b.d.	99.0
Wilbur Springs														
Micrite 1 (7)	339015	5966	2.5	6213	1136	324	41076	12128	2880	620	553	116	b.d.	116.1
Fibrous 1 (dark CL) (8)	389652	3904	1.6	148	1672	b.d.	155	16	52	72	b.d.	24	b.d.	99.0
Fibrous 2 (bright CL) (6)	389117	3443	1.4	277	1239	103	173	39	77	120	b.d.	51	b.d.	98.7
Spar 2 (orange CL) (3)	386442	1855	0.8	1156	906	101	3839	1341	389	57	b.d.	b.d.	b.d.	100.2
Spar 1 (dk orange CL) (7)	387050	3120	1.3	645	1747	62	123	13	41	34	b.d.	b.d.	b.d.	98.2
Spar 3 (yellow CL) (3)	385632	b.d.	0.0	332	270	3026	277	35	85	59	b.d.	32	b.d.	97.2
Brach shell (5)	386435	1359	0.6	268	1154	120	128	32	137	858	b.d.	170	b.d.	97.6

SD, standard deviation; CL, cathodoluminescence; dk, dark; b.d., below detection limit; el %, elemental percent.

and Ti. Consistently, high totals (>100%) obtained for these micrites were caused by a mixture of phases (microcrystalline calcite + terrigenous detrital grains), or sample inhomogeneity, at the scale of the interaction volume for the electron beam and the sample. Thus, in the detrital micrites, the iterative, matrix-correction software over-corrected the normalized (assumed homogeneous) X-ray intensities generated from what were actually different minute phases in the sample (J. Donovan, personal communication, 2001). Compared to micrite 1, yellow calcites from the Paskenta and Cold Fork sites showed a distinct drop in Fe (to 369 p.p.m.) and Mn (to 480 p.p.m.) concentrations. Both the nonluminescent, early fibrous (fibrous 1) and dentate cements were typified by relatively high Mg and Sr content, but extremely low Fe and Mn concentrations, compared to other early cements (i.e. micrite 1, yellow calcite). The recrystallized fibrous calcites (fibrous 2, yellow CL) were similar in their elemental compositions compared to the early fibrous cements from which they were derived, especially with respect to Mg, Sr and Fe concentrations, but yielded higher Mn concentrations. Isopachous and rhombohedral rim cements contained moderate amounts of Mg and Sr, but were low in Fe and Mn content compared to other carbonate phases. Finally, the late spars (1, 2, 3) displayed variable Mg, Fe and Sr contents, low S values and generally high Mn concentrations, especially for the latest spar 3 (to 3200 p.p.m. Mn) that infilled moldic porosity.

Consistent trends in Fe and Mn concentrations are evident for all three localities with respect to the paragenetic sequence (Fig. 13). Early micrites displayed moderate Mn content and high Fe concentrations, whereas all subsequent carbonate phases contained less Fe. Fibrous cements are situated at a turning point in Mn content, with near-zero values. However, Mn concentrations increazed through the various late-stage calcite spars. Early micrites of the Cold Fork and Wilbur Springs localities contained approximately twice the iron

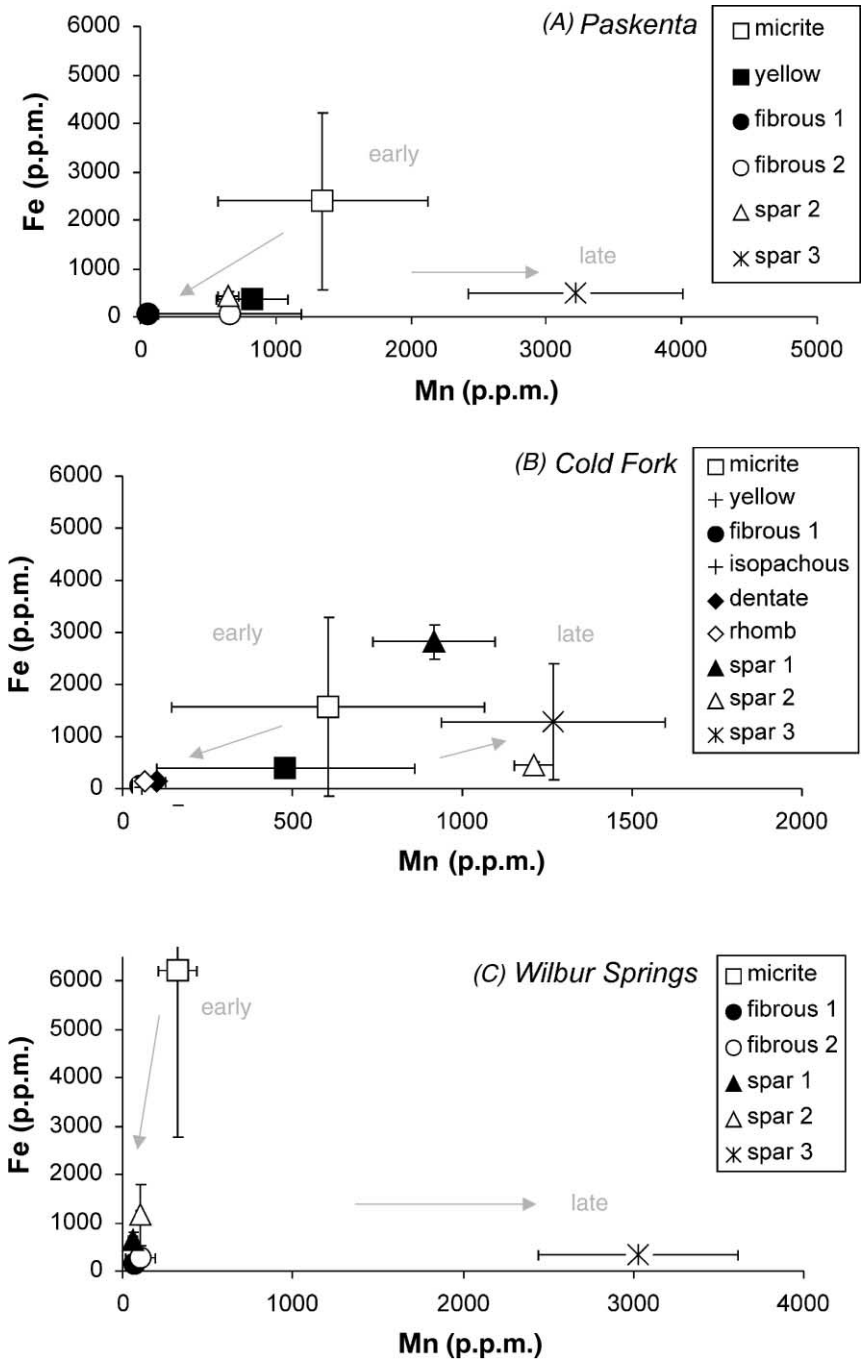

Fig. 13. Fe versus Mn concentrations for Paskenta (A), Cold Fork of Cottonwood Creek (B) and Wilbur Springs (C) seep-carbonate phases. Standard deviations about the mean values shown are graphical representations of the range of variability recorded for each cement phase.

(maximum values) compared to Paskenta early micrites, the latter also exhibiting a greater abundance of pyrite-coated corrosion surfaces.

Broadly similar patterns in Sr/Ca versus Mn and mol% Mg versus Mn are apparent for all three localities with respect to the paragenetic sequence (Figs 14 and 15). Early cements follow a distinct trend, with micrites yielding moderate Sr/Ca and Mn concentrations followed by yellow calcites with consistently lower Mn values. A shift occurred in the fibrous cement phases to relatively high Sr/Ca but extremely low Mn concentrations. A turning point in Mn content is evident in late-phase carbonates, with increased concentrations in the late spars that appear to have occurred in discrete 'jumps' with each diagenetic phase (Fig. 14), although Sr/Ca was highly variable in these late spars. All cements were preserved as low-Mg calcites (0.1–5.4 mol%). The lowest Mg content

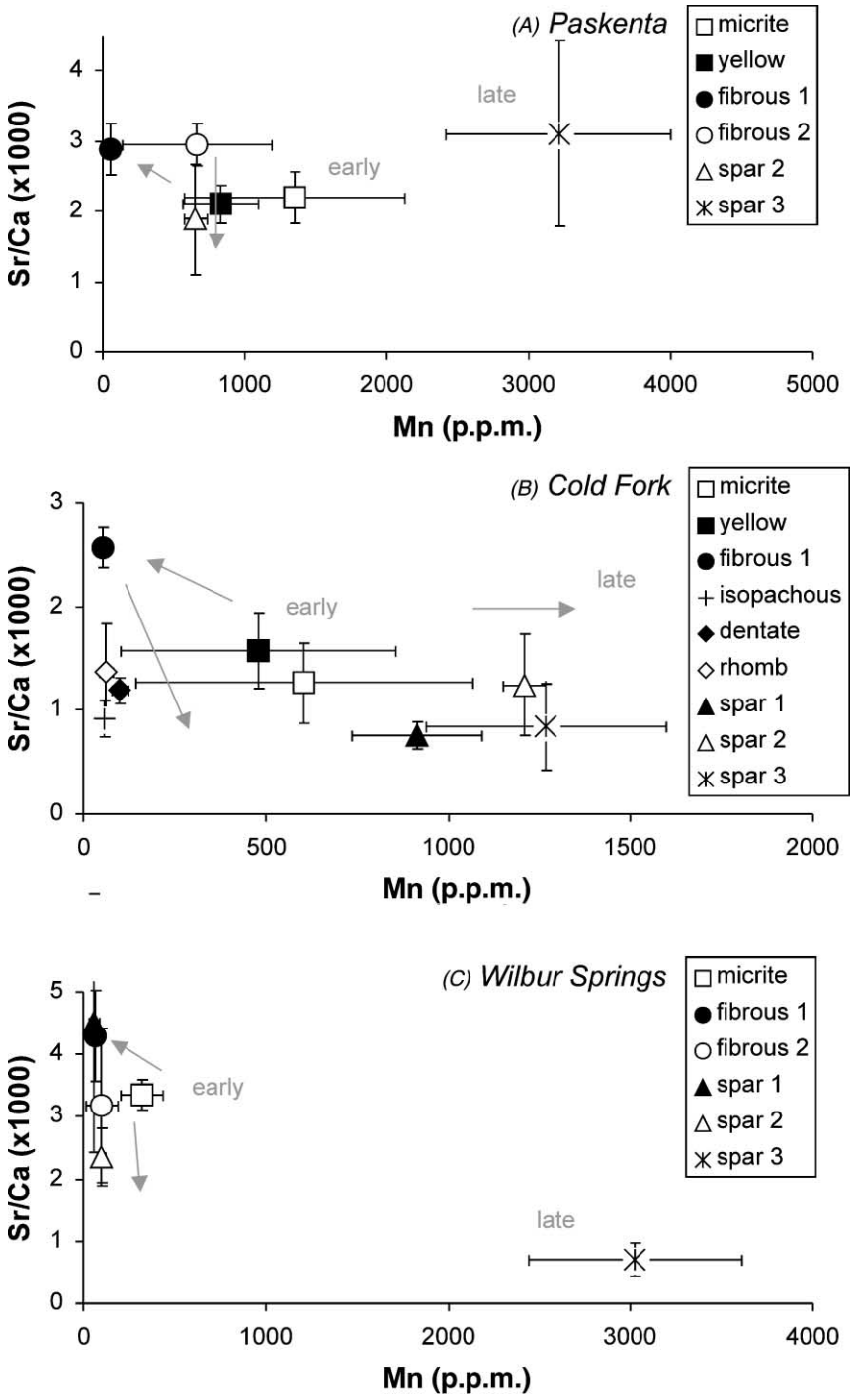

Fig. 14. Sr/Ca ratio versus Mn concentration for Paskenta (A), Cold Fork of Cottonwood Creek (B) and Wilbur Springs (C) seep-carbonate phases. Standard deviations about the mean values shown are graphical representations of the range of variability recorded for each cement phase.

occurred in the late spars, followed by increasing Mg in the yellow calcites to micrites, with Paskenta and Cold Fork fibrous cements yielding the highest Mg concentrations (Fig. 15).

Some elemental composition studies have been undertaken of other modern or ancient hydrocarbon seep-carbonates, which allow comparisons with the Californian Mesozoic data set. Botryoidal and yellow calcite cements from Canadian Arctic Mesozoic sites have approximately the same range of Mg, Sr, Mn and Na concentrations as the Californian Mesozoic examples, but with a lower Fe content (7–40 p.p.m.) (cf. Savard *et al.* 1996). The Jurassic Gateway Pass seep-limestones, Antarctica displayed Fe and Mn concentrations that were low in early fibrous cement crusts as well as in late-phase cements (Kelly *et al.* 1995). Both early and late Antarctic cements attained higher maximum Mg contents (to

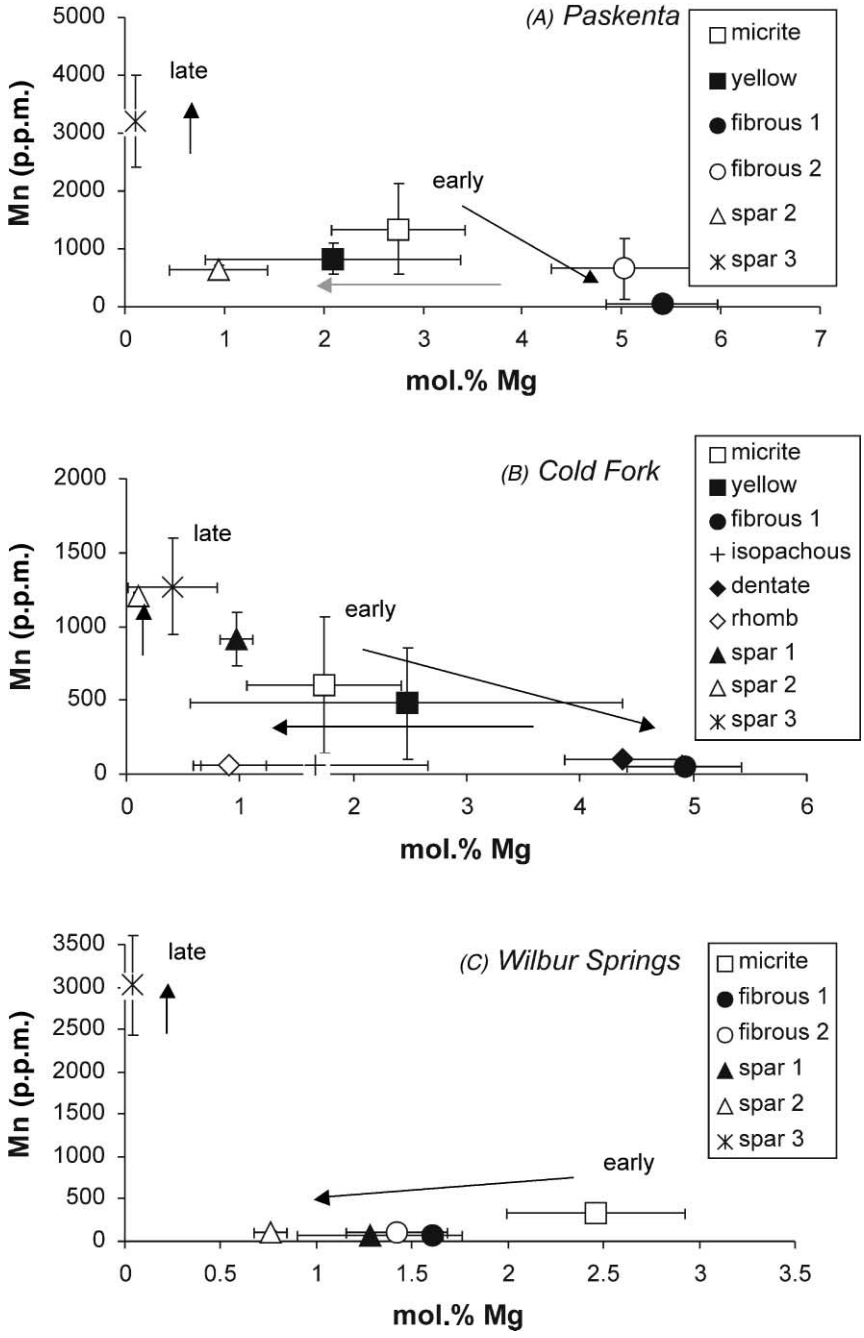

Fig. 15. Mn (p.p.m.) versus mol% Mg for Paskenta (A), Cold Fork of Cottonwood Creek (B) and Wilbur Springs (C) seep-carbonate phases. Standard deviations about the mean values shown are graphical representations of the range of variability recorded for each cement phase.

15 000 p.p.m.), attributed to high-Mg calcite precursor phases, but had similar Sr concentrations compared to Californian examples. Modern seep-carbonates from the Oregon accretionary prism (Ritger *et al.* 1987) were variable in mineralogy, but the average micritic cement was a magnesian calcite with higher Mg (12 mol%), less Fe (30–130 p.p.m.) and similar Sr concentrations compared to micrite 1 from the Californian Mesozoic deposits. Modern seep-carbonates from offshore Pakistan and in the Black Sea have higher Mg contents, and Black Sea botryoidal aragonites have high Sr and low Fe concentrations (Peckmann *et al.* 2001b, von Rad *et al.* 1996).

INTERPRETATIONS AND DISCUSSION

Conditions during early phases of seep-carbonate development

Metazoan fossils were restricted to the earliest diagenetic stage in all 14 seep-carbonate deposits identified to date from

the Mesozoic subduction system of California (Fig. 2). For both the Canadian Arctic seep-carbonates, associated with Cretaceous fault-grabens and diapirs (Beauchamp & Savard 1992), and the Californian examples most fossils were found with micrite, except for worm tubes, which were encrusted with anhedral yellow calcite in both settings. Evidence for early, sulphide-rich fluid seepage under anaerobic conditions is inferred in this study by the presence of Fe-rich, fossiliferous micrite, corrosion surfaces with pyrite coatings and anhedral yellow calcite cement. In modern hydrothermal vent and hydrocarbon seep environments, mussels and tube worms require a source of reduced fluids (rich in CH_4, H_2S) for sustenance of their internal chemosymbiotic bacteria (reviewed in Van Dover 2000). Therefore, the metazoans are distributed spatially within or around active vent-seep fields (e.g. MacDonald *et al.* 1989). Aharon (2000) described modern seep habitats as essentially anoxic enclaves surrounded by oxygen-rich bottom waters, wherein authigenic carbonates precipitate because of concentrated anaerobic methane oxidation coupled with sulphate reduction. Together, these microbially driven processes produce high levels of alkalinity and DIC in sedimentary pore fluids (Aharon 2000; Aharon *et al.* 1992; Ritger *et al.* 1987). Co-occurrence of pyrite and authigenic seep-carbonates is explained by the activities of sulphate-reducing bacteria that generate dissolved hydrogen sulphide which, in turn, reacts with iron in oxygen-poor, seafloor sediments to precipitate Fe-monosulphides that precede the formation of pyrite (e.g. Berner 1970; Wilkin & Barnes 1996, 1997).

In a model for chemosynthetic mound formation in the Canadian Arctic, Beauchamp & Savard (1992, fig. 17, p. 448) postulated that both micrite and anhedral yellow calcite precipitated beneath sulphide-oxidizing *Beggiatoa* bacterial mats under localized anaerobic conditions. However, no physical remnants of microbial features were reported for the Canadian examples. At the Cold Fork of Cottonwood Creek site in California, not only did worm tube surfaces become encrusted with anhedral yellow calcite and pyrite but, in addition, they preserved clotted micrite linings or coatings which are likely microbial in origin (e.g. Fig. 10D). The observed association between worm tubes and microbial fabrics in early diagenetic phases from California suggests that seep development in reducing microenvironments may have allowed bacterial mats to flourish, and pyrite and yellow calcite to precipitate (cf. Beauchamp & Savard 1992; Kohn *et al.* 1998). However, at all three Californian localities, microbial textures were volumetrically minor components of the seep deposits. Even considering taphonomic biases towards nonpreservation, it appears that free-living microbial mats on the seafloor were unlikely to have mediated the voluminous precipitation of micrite and yellow calcite observed in these seep deposits. It is more likely that the precipitation of these early cement phases occurred in oxygen-depleted porewaters within detrital seafloor sediments via coupled bacterial methane oxidation and sulphate reduction. The distinct microchemical conditions that controlled the precipitation of the two different reduced early cements (i.e. micrite 1 versus yellow calcite) are presently unknown, but apparently were related to H_2S-rich fluid pulses associated with CE1.

The early carbonate phases of all three Californian seep deposits revealed similar shifts in Sr/Ca versus Mn values that imply early micrite and yellow calcite formation in the presence of reducing porewaters, which was then followed by increazing water–rock interaction and fibrous 1 cement (formerly aragonite?) formation under more aerated conditions (compare Fig. 14 with Morse & Mackenzie 1990, Fig. 7.41, p. 365). The fibrous cements also exhibited elevated $\delta^{18}O$ signatures, lacked pyrite or detrital material and were bored by marine organism(s), which may indicate cement formation in association with aerobic methane oxidation by methanotrophs using oxygen dissolved in ambient (cold) bottom water (cf. Beauchamp & Savard 1992, Fig. 13, p. 444). In addition, studies of fluid flow through modern accretionary prisms have revealed that micrite slabs and lenses develop during diffuse flow through seafloor sediments, whereas ^{18}O-enriched fibrous or dentate cements commonly are associated with chimney or doughnut features that delineate advective flow in cold, ambient seafloor conditions (e.g. Kulm & Suess 1990, Ritger *et al.* 1987). We infer similar flow conditions in association with precipitation of micrite 1 and fibrous 1 cements, respectively. The spatial distribution of these two major carbonate types was studied by Campbell (1995, appendix 1, p. 195), who presented bulk-rock sampling results from transects through the Paskenta carbonate deposit. The carbonate lens margins were dominated volumetrically by micrite and fossils, but the central area of the deposit contained abundant fibrous cements and lacked fossils. This distribution may reflect diffuse fluid flow through seafloor sediments at the margins of the seep, where conditions were optimal for organism activity, and advective flow in the central area of seepage, perhaps near vents or conduits.

Conditions during late phases of burial diagenesis

The late diagenetic stage of the paragenetic sequence for Californian Mesozoic seep-carbonates is typified by pore-associated phases that recorded burial conditions, particularly the evolution or input of fluids that imply water–rock interactions distinct from either normal marine seawater or from early, hydrocarbon-rich sources. Textural, isotopic and compositional transitions are clearly indicated at the turnover point from early phases and events (1–7) to late-stage phases and events (8–18), especially for Paskenta and Cold Fork seep deposits.

Two distinct series of late-stage events are suggested by the compositional data (Figs 13–15). The first is carbonate recrystallization and/or rim cement precipitation along

cavity margins (i.e. dentate, isopachous, rhombohedral calcites) or as alteration bands across earlier phases (fibrous 2 calcites). All of these cements displayed relatively smoothly decreasing Sr and Mg contents, as compared to the preceding fibrous cements, while Fe and Mn concentrations remained similarly very low. The second series of late-stage events consisted of pore-filling precipitation (calcite spars 1–3, barite) and internal silt-clay deposition. The calcite spars exhibited low $\delta^{18}O$ values, variable Sr contents and moderately high Fe signatures. They also showed distinctive, discrete, upward shifts in Mn concentrations, and the lowest Mg concentrations of all cements. The discrete jumps in Mn content to the highest values observed suggest a return to reducing porewater conditions during burial diagenesis (compare Fig. 14 with Morse & Mackenzie 1990, Fig. 7.41, p. 365), and may reflect contributions from individual burial fluid packages with unique elemental compositions.

The three corrosion events (CE1–CE3, Fig. 5) observed during paragenesis indicate three separate shifts in fluid composition–pH during seep-carbonate development. CE1 occurred early in sediments near the seafloor, in affiliation with diffusive, relatively acidic porewaters infused with dissolved hydrogen sulphide and iron. Organisms utilized the reduced fluids of CE1 to fuel chemosynthetic energy production, and pyrite precipitated directly upon corrosion surfaces. Following CE1, an episode of advective seep fluid flow occurred, as well as contact with normal seawater, as suggested by fibrous cement characteristics (see above) and marine boring(s). During CE2, corrosion was associated with fracturing and vein formation, as well as the onset of pore-associated fluid evolution, which locally recrystallized some fibrous cements or partially dissolved micrite 2 geopetals in vugs (e.g. Fig. 6). Fracturing associated with CE2 may have occurred in relation to local tectonic events (e.g. fault movement), or by overpressuring and autobrecciation, with increasing occlusion of porosity during continued subsurface fluid flow through the deposit (cf. Conti & Fontana 1999). The final corrosion event, CE3, was marked by fabric-selective dissolution that produced secondary fenestral porosity, especially in the yellow calcites. Corrosion was driven by input of burial fluids that were undersaturated in bicarbonate.

In general, mineral-diagenetic stabilization of carbonates typically proceeds in discrete microenvironments (Veizer 1983). Newly precipitated phases form via fluid input and/or localized dissolution–reprecipitation of precursor carbonate components (cf. Bathurst 1975). The latter process buffers the incoming fluids to partially preserve individual internal phases and their varying compositional gradients (Veizer 1983). Once the metastable mineral–textural assemblage has been transformed to low-Mg calcite, and residual porosity has become occluded, carbonates generally behave as a closed diagenetic system (Veizer 1983). Thus, the distinctive textural–isotopic–elemental characteristics of the Californian Mesozoic seep-carbonates record a rich birth-to-burial history of these unusual deposits and their faunas, and also reveal aspects of hydrogeological evolution not preserved elsewhere in the Franciscan–Great Valley arc–trench system.

Phanerozoic trends in stable isotopic signatures of seep-carbonates

Figure 16 illustrates the range of stable carbon and oxygen isotopic distributions of 33 reported deposits of authigenic marine carbonates which precipitated in association with submarine fluid seepage from Phanerozoic continental margins and epicontinental seaways around the world. These include 14 modern, nine Cenozoic and 10 Palaeozoic–Mesozoic seep-carbonate occurrences for which stable isotopes have been measured. Table 4 lists the complete data set and literature references for each occurrence, whereas Fig. 16 displays general trends and highlights only selected localities. Three broad stable isotopic fields are delineated (Fig. 16): (i) a ^{13}C-, ^{18}O-depleted field containing most Mesozoic and Palaeozoic seep-carbonates (Group I); (ii) a variably ^{13}C-depleted, but ^{18}O-enriched field, constituting most Cenozoic and modern seep-carbonates (Group II); and (iii) a scattered, ^{13}C-enriched field, with ^{18}O content ranging from depleted to enriched (Group III).

Mesozoic sites from California (Fig. 16) are situated in the depleted ^{18}O–^{13}C quadrant (Group I), along with most other Palaeozoic and Mesozoic seep-carbonate deposits. However, compared to most of these examples, the Paskenta carbonates were relatively more depleted in ^{13}C, and all three Californian deposits were relatively more enriched in ^{18}O. The exceptional occurrence in this quadrant is from the modern Oregon deformation front (OrDF), where carbonate cements and veins associated with vertical faults were exceptionally depleted in ^{18}O, and overlapped with Cold Fork and Paskenta oxygen values (Fig. 16). For the OrDF, the unusual isotopic signatures of these modern seep-carbonates were explained by tapping of deep, warm fluids during active faulting, and by recrystallization of terrestrial clay minerals (Sample *et al.* 1993; Sample & Reid 1998). Other Mesozoic seep deposits from Antarctica, Colorado and the Canadian Arctic (Fig. 16) had somewhat similar isotopic signatures compared to the Californian sites. However, their late phases were more strongly depleted in ^{18}O (Table 4), perhaps explained by higher formation temperatures and/or distinctive fluids associated with burial diagenesis. An isotopically unusual Mesozoic seep deposit was reported from calcitic micrites of the late Jurassic Terres Noires Formation, southern France (Fig. 16, Group III), which exhibited a widely variable range of $\delta^{13}C$ values (-26.5 to $+15$‰ PDB), and low to slightly elevated $\delta^{18}O$ values (approximately -7 to $+1$‰ PDB) (Peckmann *et al.* 1999a). The exceptionally ^{13}C-enriched carbonate carbon content of the French examples was attrib-

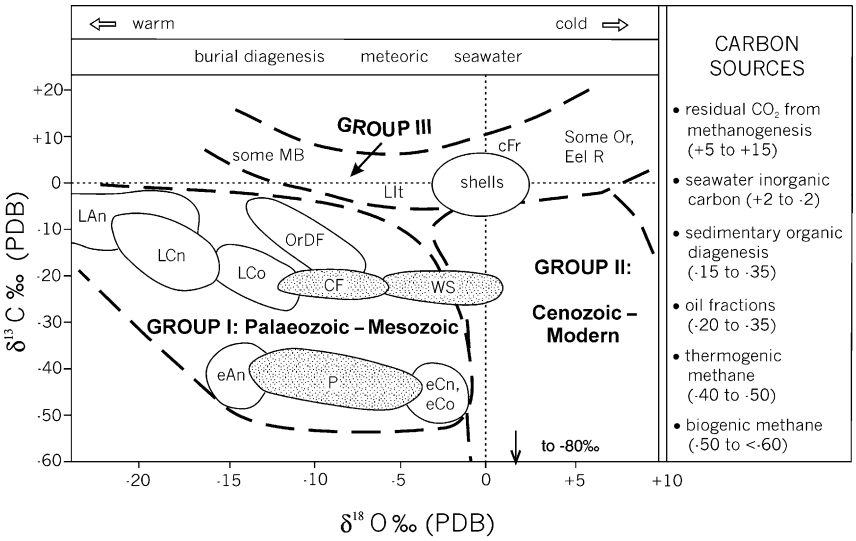

Fig. 16. Carbon and oxygen stable isotopic signatures for 33 Phanerozoic seep-carbonates world-wide. Data set and literature references for the plotted 14 modern, nine Cenozoic and 10 Mesozoic–Palaeozoic occurrences are shown in Table 4. With few exceptions, data clustered in three fields: Group I, Palaeozoic–Mesozoic seep-carbonates; Group II, Cenozoic–Modern seep-carbonates; Group III, scattered outliers. Unaltered, seep-associated shell-carbonate values are aggregated about 0‰ PDB for both carbon and oxygen. Paskenta (P), Cold Fork of Cottonwood Creek (CF) and Wilbur Springs (WS) data from this study are stippled. Shown for comparison with the isotopic signatures of global seep-carbonates are potential carbon isotope sources (vertical, at far right; Deines 1980), and various influencing factors (i.e. temperature and/or ^{18}O composition of fluids) on oxygen isotopes (horizontal, across top; Anderson & Arthur 1983; Land 1989; Veizer 1983). DF = deformation front; e = early cement; L = late cement; Or = modern Oregon; Eel R = modern Eel River; MB = modern Monterey Bay; It = Italy (Miocene); Cn = Canadian Arctic (Cretaceous); Co = Colorado (Cretaceous); cFr = calcitic French carbonates (Jurassic); An = Antarctica (Jurassic).

uted to equilibration with CO_2 produced during bacterial methanogenesis (Gaillard *et al.* 1992).

One factor that could explain the clustering of most Palaeozoic and Mesozoic seep-carbonate deposits in a ^{13}C-, ^{18}O-depleted isotopic field (Group I, Fig. 16) is post-depositional dissolution and reprecipitation during burial diagenesis. Although $\delta^{13}C$ signatures of carbonate cements are generally somewhat resistant to modification (cf. Aharon 2000), this process can decrease $\delta^{18}O$ values markedly, even at low water–rock interactions, as illustrated in studies of normal marine and burial carbonates (e.g. Allan & Matthews 1977; Given & Lohmann 1985; Patterson & Walter 1994; Veizer 1983). Seep-carbonates, in particular, form as small deposits from point sources of hydrocarbon seepage in basins dominated volumetrically by siliciclastic sediments. Dewatering of these enclosing clastics during burial would have subjected the carbonates to the passage of large volumes of porewater. The combined effects of time and elevated temperatures likely promoted isotopic exchange between these older seep-carbonates and incoming pore fluids, and thus might have modified substantially the $\delta^{18}O$ values of some phases (cf. Veizer 1983). Nonetheless, clear isotopic and elemental trends are still preserved in many Palaeozoic and Mesozoic seep-carbonate phases (e.g. Figs 12–15; cf. Kauffman *et al.* 1996, Fig. 4, p. 801; cf. Veizer 1983, p. 285–287), despite the overall negative shift in Group I $\delta^{18}O$ values compared to Cenozoic and modern seep-carbonates. For example, early and late diagenetic phases are recorded as distinct oxygen isotopic subgroups in many Group I seep-carbonates (e.g. e vs. L subfields, respectively, Fig. 16). Alternatively, the systematically low $\delta^{18}O$ values of Palaeozoic and Mesozoic seep-carbonates may reflect secular variations in seawater oxygen isotopic composition and/or temperatures through Earth's history, as has been suggested to explain the same pattern found in pre-Jurassic marine sedimentary deposits world-wide (cf. Lécuyer & Allemand 1999, p. 357–359). Nonetheless, oxygen isotopic signatures of shell-carbonate from the Californian Mesozoic seep-carbonates (Fig. 11) are consistent with modern seawater values, and show no significant depletion in ^{18}O content.

In the second stable isotopic field (Group II, Fig. 16), most Cenozoic and modern seep-carbonates yielded $\delta^{18}O$ values between ~0 and +10‰ PDB, and formed in cold waters at shelf to slope depths (see Table 4 for details). In addition, some deposits were associated with gas hydrates. The enriched oxygen isotopic signatures of these younger deposits suggest that they were subjected to less alteration by time–temperature-dependent diagenetic processes, in comparison to the older Group I seep-carbonates. The $\delta^{13}C$ values of Cenozoic and modern seep-carbonates ranged from approximately −80 to −10‰ PDB, and are attributed to variable carbon reservoirs of increasing ^{12}C content, i.e. imprinted by processes of biogenic or thermogenic methane oxidation, crude oil leakage and/or sedimentary organic matter diagenesis (compare Fig. 16 with Roberts & Aharon 1994, Fig. 9, p. 146).

Table 4 Global data set of stable carbon and oxygen values for 33 Phanerozoic seep-carbonates reported from the literature. Includes 14 modern citations, 9 Cenozoic occurrences and 10 Mesozoic–Paleozoic occurrences; where reported, isotopic ranges for individual mineralogic phases are indicated.

Location	Geotectonic/ stratigraphic context	Age	Morphology of carbonate deposits	Carbonate mineralogy, sedimentology	δ^{13}C‰ (PDB) range per component	δ^{18}O‰ (PDB) range per component	Reference
Offshore eastern Aleutians, Gulf of Alaska	Convergent/ accretionary prism; vertical shear faults	Modern	Crusts, cemented sediment, chimneys	Micrite (HMC):			Suess *et al.* (1998)
				Edge site	−10.7 to −14.3	+1.1 to +2.9	
				Shumagin site	−45.9 to −50.8	+2.1 to +3.2	
Offshore Oregon, USA	Convergent/trans-form faults, thrust ridges, Cascadia accretionary prism	Modern	Cemented sediments, slabs, veins, chimneys, doughnuts	*Population I*:			Bohrmann *et al.* (1998), Goldfinger *et al.* (1999), Kulm & Suess (1990), Kulm *et al.* (1986), Ritger *et al.* (1987), Sample & Kopf (1995), Sample & Reid (1998), Sample *et al.* (1993)
				Micrite (MHC)	−32.5 to −54.8	+3.2 to +6.8	
				Micrite (calcite)	−18.7 to −53.4	−5.9 to +5.7	
				Aragonite	−50.0 to −53.3	+3.7 to 4.4	
				Population II:			
				Undiff. HMC, calcite, dolomite	−1.0 to −25	−5.5 to −12.9	
				Population III:			
				Micrite (dolomite)	−16.0 to −21.9	+7.3 to +7.9	
				Population IV:			
				Undifferentiated	−1.9 to 25.9	+0.7 to +10.7	
Eel River Basin, offshore northern California, USA	Convergent/mud volcanoes, anticlines, gas hydrates	Modern	Not reported	Aragonite, HMC, dolomite	+9 to −40 undifferentiated	+3.2 to +6.6 undifferentiated	Lorenson *et al.* (1999), Naehr & Stakes (1999)
Monterey Bay, California, USA	Transpressive/transform faults	Modern	Cemented sediment, chimneys, doughnuts, veins, concretions	HMC micrite	−30 to −56	+4 to +7	Naehr & Stakes (1999), Stakes *et al.* (1999)
				Dolomite micrite	−52.6 to +9.6	−12.9 to +6.8	
				Calcite ccc micrite	−46 to −55.6	+3.5 to +6.3	
				Calcite veins	+9.5	−7.2	
Guaymas Basin, Gulf of California	Transform margin/fault on slope	Modern	Ledges, pockmark rims	Aragonite	−36 to −38.1	+4.2 to +4.8	Simoneit *et al.* (1990)
Gulf of Mexico, USA	Passive/salt diapirs, faults, mud volcanoes, brine pools	Modern	Mounds, nodules, slabs, ledges, chimneys ± breccia, gas hydrate	Micrite (HMC)	−9.5 to −55	+2 to +5.5	Aharon *et al.* (1997), Ferrell & Aharon (1994), Roberts & Aharon (1994), Roberts *et al.* (1990)
				Aragonite	−23.5 to −55	Not reported	
				Dolomicrite	−30.4 to −53.8	Not reported	
Florida Escarpment, USA	Passive/platform brine-seawater circulation	Modern	Crusts, nodules at base of Escarpment	Micrite + coarse spar (calcite)	−5 to −48.5, bulk values	+1.6 to +4.4, bulk values	Coston (1989), Neumann *et al.* (1988), Paull *et al.* (1991, 1992)
				Pelagic carbonate dissolution	+2 to −15	+1.5 to −3.4	

Table 4 continued

Location	Geotectonic/ stratigraphic context	Age	Morphology of carbonate deposits	Carbonate mineralogy, sedimentology	$\delta^{13}C$‰ (PDB) range per component	$\delta^{18}O$‰ (PDB) range per component	Reference
Offshore Norway, Northe Sea	Rift/sediment-draped grabens	Modern	Pockmark associated hardground pavements	Micrite (HMC-cements in ss) Aragonite Aragonite + calcite	Not reported −54.0 to −61.1 −36.3 to −57.2	Not reported +1.9 to +4.7 Not reported	Hovland & Judd (1988), Hovland *et al.* (1987)
Offshore Pakistan	Convergent/Makran accretionary prism	Modern	Irregular, dark grey to black crusts	Micrite (HMC, Ca-rich dolomite)	−36.1 to −44.8	+1.2 to +2.6	von Rad *et al.* (1996)
Offshore eastern New Zealand	Convergent/Hikurangi accretionary prism; slumps, diapirs	Modern	Slabs, nodules, chimneys	Dolomite 'Cement' fill	−4.9 to −12.8 −39.2	+4.9 to +5.4 Not reported	Lewis & Marshall (1996), Orpin (1997), Pantin (1957)
Outer Mariana Trough	Convergent/non-accretionary forearc seamounts	Modern	Chimneys, crusts on serpentinite diapirs	Aragonite Pore-fill HMC Spar overgrowths (calcite)	−1.2 to −21.2 Not reported −10.9 to −11.8	+4.5 to +7.6 Not reported +6.0 to +6.3	Haggerty (1987, 1991)
Nankai Trough, Sagami Bay, Japan	Convergent/thrusts in accretionary wedge	Modern	Slabs, pipes; cemented stones, shells, sandstone	Micrite (Mg-rich to HMC) Calcite + minor aragonite (Nankai)	−27.2 to −56 −40 to −44	+2.5 to +5.7 +2.5 to +4.5	Hattori *et al.* (1994), Henry *et al.* (1999), Sakai *et al.* (1992)
Northwestern Black Sea, Romanian shelf & Ukranian slope	Extensional/ voluminous sediment loading	Modern	Crusts, chimneys, platforms	Micrite (HMC) Aragonite	−27 to −41 −26 to −38	+0.2 to +1.2 Undiff.	Peckmann *et al.* (2001b), Peckmann personal communication 2001
Offshore Russia adjacent to Paramushir and Sakhalin Islands, Sea of Okhotsk	Transpressive/ unstable gas hydrates; highs (volcanic/structural); along faults, Sakhalin Shear Zone	Holocene–Pleistocene	Irregular crusts, slabs, concretions, nodules and pockmark rims above gas hydrate	Micrite (HMC)	−25.8 to −49.2	+2.9 to +3.9	Baranov *et al.* (1999), Derkachev *et al.* (1999), Greinert *et al.* (1999), Lein *et al.* (1989), Lorenson *et al.* (1999), Zonenshayn *et al.* (1987)
Yokohama City, Kanagawa Prefecture, central Japan	Convergent	Lower Pleistocene, Kazusa Group	Concretions, burrow fills, cemented shells	Micrite	−55	Not reported	Majima *et al.* (1996)
Kimitsu City, Chiba Prefecture, Boso Peninsula, central Japan	Convergent/ outer shelf	Middle Pleistocene, Kazusa Group	Cemented burrows/shells + pipe-like concretions	Micrite Acicular calcite	−48.8 to −62.3 −58	+2.6 to +4.1 +2.6	Shibasaki & Majima (1997)
Quinault coast, Washington, USA	Convergent/ Cascadia forearc	Pliocene, Quinault Fm.	Burrow/shell-fill, blebs	Micrite	−14.0 to −33.6	+0.9 to +2.2	Campbell (1992)

Table 4 continued

Location	Geotectonic/ stratigraphic context	Age	Morphology of carbonate deposits	Carbonate mineralogy, sedimentology	$\delta^{13}C‰$ (PDB) range per component	$\delta^{18}O‰$ (PDB) range per component	Reference
Northern East Coast Basin, North Island, New Zealand	Convergent/ Hikurangi forearc	Lower to Upper Miocene	Mounds, pipes, nodules	Micrite (calcite) Fibrous aragonite	−29.9 to −49.2 −45.0 to −51.7	−5.0 to +2.4 +0.7 to +2.7	Campbell & Francis (1998), Campbell *et al.* (1999), unpublished data
Tuscan-Romagna Appenines, Italy	Concurrent subduction, thrusting	Lower–Upper Miocene, calcari a *Lucina* limestone	Breccias, nodular, doughnut, veins	Micrite >20% dolomite Aragonite veins, botryoids 'Meteoric'	−16 to −52 Not reported −40 to −58 +2 to −16	−5 to +2.5 +1.5 to +5 Not reported −3 to −11	Conti & Fontana (1999), Terzi *et al.* (1994)
Marmorito, northern Italy	Episutural basin developed on old accretionary prism	Miocene	Marly fossilif. limestone, cemented clastics cross-cut by veins	Micrite Dolomitic matrix Fibrous aragonite Calcite veins, neo-morphosed matrix	−26 to −35 −39 to −40 −26 to −35 −17 to −28	−0.5 to +4.9 +3.5 to +4 +0.3 to +2.8 +1.4 to +2.1	Clari *et al.* (1988, 1994), Peckmann *et al.* (1999a)
Santa Cruz, California, USA	Transpressive/ strike–slip faults, San Gregorio Fault Zone	Upper Miocene, Santa Cruz Mudstone	Slabs, pipes, concretions, massive mounds	Micrite (calcite)	−4.5 to −13.8	−1.8 to +0.8	Aiello *et al.* (1999)
North Slope, Alaska, USA	Foreland/anticline	Oligocene or Pliocene, Nuwork Mbr., Sagavanirktok Fm.	Nodules, beds; associated with glendonite	Micrite (HMC) Spar (calcite)	−30 to −69 −31 to −46	+1.7 to +3.2 +0.9 to +1.4	Campbell *et al.* (2000), unpublished data
Juan de Fuca straits, Washington, USA	Convergent	Lower Oligocene, Makah Fm.	Allochthonous blocks, from up-slope	Micrite Fibrous cement Spar (calcite)	Not reported −26.2 to −34.5 Not reported	Not reported −0.8 to −2.9 Not reported	Goedert & Campbell (1995)
Tepee Buttes, Colorado, USA	Epeiric seaway/ basement faults, early Laramide orogeny	Upper Cretaceous (Campanian)	Mounds, pipe-like core; irregular nodules	Micrite peloids Fibrous cement Late spar	−42 to −46 −35 to −43 −12 to −29	0 to −2.5 −1.8 to −5.5 −7.5 to −14	Arthur *et al.* (1982), Howe (1987), Kauffman *et al.* (1996)
Canadian Arctic Islands	Sverdrup Basin; faults associated with salt diapir or half-graben	Lower Cretaceous (Aptian–Albian), Christopher Fm.	Mounds	*Early calcites*: Botryoidal Micrite Splayed Yellow *Late cements*: Bladed calcite Xeno dolomite	 −36 to −50 −37 to −43 −36 to −50 −35 to −42 −8 to −25 all Undifferentiated	 −0.1 to −1.8 +1.5 to −5 all Undifferentiated −12 to −20 all Undifferentiated	Beauchamp & Savard (1992), Beauchamp *et al.* (1989), Savard *et al.* (1996)

Table 4 continued

Location	Geotectonic/ stratigraphic context	Age	Morphology of carbonate deposits	Carbonate mineralogy, sedimentology	$\delta^{13}C$‰ (PDB) range per component	$\delta^{18}O$‰ (PDB) range per component	Reference
Cold Fork of Cottonwood Creek, California, USA	Convergent/ synsedimentrary faults in forearc basin	Lower Cretaceous (Aptian–Albian), Great Valley Group	Lenses, nodules	*Early calcites*: Micrite Yellow Fibrous Late calcite: Spar (undiff.)	 −24.9 −20.6 to −21.4 −20.1 to −23.4 −20.3	 −7.4 −8.0 to −8.9 −3.0 to −4.3 −11.3	This paper
Wilbur Springs, California, USA	Convergent/ atop serpentine diapirs in forearc basin	Lower Cretaceous (Hauterivian), Great Valley Group	? (quarried)	*Early calcites*: Micrite Fibrous Late calcite: Spar (undiff.)	 −19.3 to −22.2 −21.3 to −24.3 −19.4 to −21.8	 −0.5 to +1.8 +1.1 to +2.3 +0.8 to −5.2	This paper
Paskenta, California, USA	Convergent/ synsedimentary faults in forearc basin	Upper Jurassic (Tithonian), Great Valley Group	Lens	*Early calcites*: Micrite Yellow Fibrous Late calcite: Spar (undiff.)	 −32.1 to −35.5 −32.4 to −38.0 −34.4 to −43.7 −27.9 to −38.4	 −7.8 to −10.8 −6.5 to −9.8 −0.9 to −3.9 −12.8 to −13.8	This paper
Alexander Isaland, Antarctica	Convergent/ forearc basin fault	Upper Jurassic (Tithonian), Fossil Bluff Group	Crusts, cemented sediments	*Early calcites*: Fibrous Microspar geopetal Late calcites: Blocky spar	 −40.8 to −44.6 −33.5 to −40.5 −3 to −13	 −12.7 to −15.3 −12.7 to −15.3 −15 to −27	Kelly *et al.* (1995)
Beauvoisin, southeastern France	Extensional/ subsiding basin marginal to extensional Ligurian Tethys; fault associated	Upper Jurassic (Oxfordian), Terres Noire Fm.	Mounds, lenses, nodules, concretions	Micrite (calcite) Botryoidal aragonite Undiff. carbonates	−26.5 to +13 −14.8 to −12 −13.6 to +15.1	−0.5 to +2.9 −7.1 to −6.6 −1.2 to +0.7	Gaillard *et al.* (1992), Peckmann *et al.* (1999a)
Harz Mountains, Germany	Drowned rift-basin seamount (Iberg reef-atoll) on ?volcanic high	Lower Carboniferous (Visean)	In Neptunian dikes, in lows on dead reef surface	Fossilif. micrite (dolomite, calcite) Isopachous Microbial/botryoid Late calcite spar	−10 to −7.5 −25.2 to −12.8 −32.0 to −17.2 −12.9 to −3.4	∼−12 to ∼−10 ∼−11 to ∼−7 ∼−10 to ∼−7 −13.4 to −12.6	Peckmann *et al.* (2001a)
Hamar Laghdad, Antiatlas, Morocco	Epeiric/submarine rise and associated neptunian dikes	Middle Devonian (Eifelian–Givetian)	Mum mound (Hollard Mound)	*Early cements*: Micrite/clotted Rim cement (calcite) Late cement: Rhombohedral (Fe-calcite)	 −1 to −11 −16 to −20 −7 to −11	 −1 to −17 −3 to −5 −3 to −13	Peckmann *et al.* (1999b, 2000)

HMC, high-Mg calcite; ccc, crusts, chimneys, concretions; fossilif., fossiliferous; undiff., undifferentiated; xeno, xenomorphic; Fm., Formation; Mbr., Member.

Several distinct outlier carbonate types with elevated $\delta^{13}C$ and highly variable $\delta^{18}O$ signals constitute the third stable isotopic field (Group III, Fig. 16). These scattered, isotopically unusual carbonates include some modern Oregon dolomite chimneys and Eel River seep-carbonates with isotopically heavy carbonate carbon, attributed to CO_2 sources enriched in ^{13}C by methanogenesis (c.f. Kulm & Suess 1990; Lorenson *et al.* 1999; Roberts & Aharon 1994). In addition, some seep-carbonates from the modern Eel River basin display elevated $\delta^{18}O$ values, attributed to formation in association with gas hydrate decomposition (e.g. Lorenson *et al.* 1999; Naehr & Stakes 1999). Finally, some Group III precipitates with depleted $\delta^{18}O$ signatures were inferred to have formed under meteoric influences, e.g. some Miocene late diagenetic cements from Italy and some modern Monterey Bay veins (Fig. 16; Naehr & Stakes 1999; Stakes *et al.* 1999; Terzi *et al.* 1994).

In summary, Californian Mesozoic seep-carbonates of this study are differentiated from one another isotopically, but fall into the broad range of depleted ^{13}C–^{18}O contents typical of most other Palaeozoic–Mesozoic seep-carbonates worldwide. These older seep-carbonates clearly preserved a distinct signal of early, hydrocarbon-derived cement phases. However, their relatively low $\delta^{18}O$ values indicate a strong diagenetic overprint, likely related to their older age and therefore increased probability of having experienced significant modification during burial. In contrast, most Cenozoic and modern seep-carbonates were: (i) isotopically distinct from the older deposits; (ii) recorded variable hydrocarbon sources and generally ambient seafloor conditions; and (iii) contained less evidence for significant post-depositional isotopic alteration. Finally, fluids enriched in residual CO_2, or fluids charged with meteoric waters, have occasionally formed seep-carbonates in marine settings, but their relations to hydrocarbon formation and migration, if any, have not yet been studied in any detail.

CONCLUSIONS

Three studied seep-carbonate occurrences in Great Valley forearc strata (Upper Jurassic to Upper Cretaceous, turbidite/fault-hosted or serpentine diapir-related), California, contain 18 recurring paragenetic events/phases. Stable isotope values and elemental compositions of the carbonates co-varied with respect to carbonate phase, and these patterns tracked the onset and development of seafloor seepage, followed by late-stage fluids introduced during burial diagenesis. Despite significant water–rock interactions among discrete fluids in particular microenvironments, original (or partially modified) textures and chemical gradients were well preserved in these Mesozoic seep-carbonates. At each site, fossil mega-fauna, some chemosymbiotic, were restricted to the early stages of seep development, and they maintained contact with sulphide-, petroleum- and/or methane-rich fluids near the sediment–water interface. Microbial activity is suggested by nondetrital micrite, with finely laminated and clotted textures, which appears to have persisted longer than the mega-invertebrate activity in these seep palaeoenvironments. A broadly consistent pattern in cement stratigraphy for both Canadian Arctic and Californian Mesozoic seep occurrences implies that fluid generation processes and porewater evolution were similar for these two geographically and tectonically disjunct hydrocarbon seep settings.

Late diagenetic stage events in the Californian seep-carbonates were recorded in pores, and constituent phases delineated the loss of contact with normal seawater conditions due to increasing burial. Two divisions of this late stage are apparent: (i) corrosion and recrystallization/reprecipitation of vug-rim carbonate cements; and (ii) later, pore-occluding fill by barite, three varieties of spar, and silt-clay. Elemental compositions underwent relatively smooth transitions in the former grouping of carbonate phases, but changed in discrete shifts/jumps in the latter, suggesting inputs of distinct fluid packages during late diagenesis.

Global comparisons of stable isotopic signatures for 33 Phanerozoic, authigenic carbonates associated with submarine fluid seepage define three distinct fields, with Californian examples of this study plotting with the older Palaeozoic–Mesozoic deposits. In general, the younger the seep deposit, the less likely that time–temperature-dependent burial diagenesis will have left an overprint on oxygen isotopic signatures. Carbon sources for Phanerozoic sites as a whole were variable isotopically but are inferred to have been affected by petroleum migration, diagenesis of sedimentary organic matter and other diagenetic processes. Several carbonate deposits display outlier isotopic signatures, attributed to CO_2-rich or freshened fluids in offshore (palaeo)environments.

ACKNOWLEDGEMENTS

We acknowledge financial support to K.A.C. from the Petroleum Research Fund of the American Chemical Society, administered through the Department of Earth Sciences, University of Southern California; a National Research Council Research Associateship, administered through NASA Ames Research Center; and the University of Auckland Research Committee. J.D.F. received support from NASA's Exobiology Program and the NASA Astrobiology Institute. D.J.D. received support from the NASA Astrobiology Institute. A. C. Alfaro and L. Cotterall contributed drafting expertise. Field and/or laboratory assistance was provided by D. J. Bottjer, M. Campbell, L. Campbell, M. Discipulo, J. J. Donovan, B. W. Fouke and J. Goedert. For fruitful discussions, we thank D. J. Bottjer, C. Carlson, J. J. Donovan, A. G. Fischer, B. W. Fouke, T. L. Ku, C. T. S. Little, D. L. Orange and K. A. Rodgers. J. Peckmann and R. Worden made helpful suggestions that improved the quality of the manuscript.

REFERENCES

Aharon P (1994) Geology and biology of modern and ancient submarine hydrocarbon seeps and vents: an introduction. *Geo-Marine Letters*, **14**, 69–73.

Aharon P (2000) Microbial processes and products fueled by hydrocarbons at submarine seeps. In: *Microbial Sediments* (eds Riding RE, Awramik SM), pp. 270–81. Springer-Verlag, Berlin.

Aharon P, Graber ER, Roberts HH (1992) Dissolved carbon and $\delta^{13}C$ anomalies in the water column caused by hydrocarbon seeps on the northwestern Gulf of Mexico slope. *Geo-Marine Letters*, **12**, 33–40.

Aharon P, Schwartz HP, Roberts HH (1997) Radiometric dating of submarine hydrocarbon seeps in the Gulf of Mexico. *Geological Society of America Bulletin*, **109**, 2–13.

Aiello IW, Stakes DS, Kastner M, Garrison RE (1999) Carbonate vent structures in the Upper Miocene Santa Cruz Mudstone at Santa Cruz, California. In: *Late Cenozoic Fluid Seeps and Tectonics Along the San Gregorio Fault Zone in the Monterey Bay Region, California, Volume & Guidebook GB-76* (eds Garrison RE, Aiello IW, Moore JC), pp. 35–51. Pacific Section, American Association of Petroleum Geologists, Bakersfield, California.

Allan JR, Matthews RK (1977) Carbon and oxygen isotopes as diagenetic and stratigraphic tools: surface and subsurface data, Barbados, West Indies. *Geology*, **5**, 16–20.

Anderson FM (1945) Knoxville series in the California Mesozoic. *Geological Society of America Bulletin*, **56**, 909–1014.

Anderson TF, Arthur MA (1983) Stable isotopes of oxygen and carbon and their application to sedimentologic and paleoenvironmental problems. In: *Stable Isotopes in Sedimentary Geology, Society of Economic Paleontologists and Mineralogists Short Course*, **10**, 1–51. SEPM, Tulsa, Oklahoma.

Armstrong JT (1988) Bence-Albee after 20 years: review of the accuracy of α-factor correction procedures for oxide and silicate minerals. In: *Microbeam Analysis* (ed. Newbury DE), pp. 469–76. San Francisco Press Inc., San Francisco.

Arthur MA, Kauffman EG, Scholle PA, Richardson R (1982) Geochemical and paleobiological evidence for the submarine spring origin of carbonate mounds in the Pierre Shale (Cretaceous) of Colorado. *Geological Society of America, Abstracts with Programs*, **14**, 435.

Bailey EH, Irwin WP, Jones DL (1964) Franciscan and related rocks and their significance in the geology of western California. *California Division of Mines Geological Bulletin*, **183**, 1–171.

Bailey EH, Jones DL (1973) Preliminary lithologic map, Colyear Springs quadrangle, California. *US Geological Survey Miscellaneous Field Studies*, **MF-516**.

Baranov B, Suess E, Wong HK, Karp BY (1999) Tectonic pattern offshore of the Sakhalin shear zone: implications on seep distribution. *American Association of Petroleum Geologists, Pacific Section Convention Program*, 22–3.

Bathurst RCG (1975) *Carbonate Sediments and Their Diagenesis*, pp. 1–658. Elsevier, Amsterdam.

Beauchamp B, Krouse HR, Harrison JC, Nassichuk WW, Eliuk LS (1989) Cretaceous cold-seep communities and methane-derived carbonates in the Canadian Arctic. *Science*, **244**, 53–6.

Beauchamp B, Savard M (1992) Cretaceous chemosynthetic carbonate mounds in the Canadian Arctic. *Palaios*, **7**, 434–50.

Berkland JO (1973) Rice Valley outlier — new sequence of Cretaceous–Paleocene strata in Northern Coast Ranges, California. *Geological Society of America Bulletin*, **84**, 2389–406.

Berner RA (1970) Sedimentary pyrite formation. *American Journal of Science*, **268**, 1–23.

Bohrmann G, Greinert J, Suess E, Torres M (1998) Authigenic carbonates from the Cascadia subduction zone and their relation to gas hydrate stability. *Geology*, **26**, 647–50.

Campbell KA (1992) Recognition of a Mio-Pliocene cold seep setting from the northeast Pacific convergent margin, Washington, USA. *Palaios*, **7**, 422–33.

Campbell KA (1995) Dynamic development of Jurassic–Pliocene cold-seeps, convergent margin of western North America. PhD Thesis. University of Southern California, Los Angeles.

Campbell KA (1996) Gastropods of Mesozoic cold-seep carbonates, California. *Geological Society of America, Abstracts with Programs*, **28**, A298.

Campbell KA, Aharon P, Marincovich L Jr (2000) Paleo-gas hydrates in the Arctic Ocean: evidence from Late Neogene Nuwok strata, northern Alaska. *Geological Society of America, Abstracts with Programs*, **32**, A102.

Campbell KA, Bottjer DJ (1993) Fossil cold seeps (Jurassic–Pliocene) along the convergent margin of western North America. *National Geographic Research and Exploration*, **9**, 326–43.

Campbell KA, Bottjer DJ (1995a) Brachiopods and chemosymbiotic bivalves in Phanerozoic hydrothermal vent and cold-seep paleoenvironments. *Geology*, **23**, 321–4.

Campbell KA, Bottjer DJ (1995b) *Peregrinella*: an Early Cretaceous cold-seep-restricted brachiopod. *Paleobiology*, **21**, 461–78.

Campbell KA, Carlson C, Bottjer DJ (1993) Fossil cold seep limestones and associated chemosymbiotic macroinvertebrate faunas, Jurassic–Cretaceous Great Valley Group, California. In: *Advances in the Sedimentary Geology of the Great Valley Group, Book no. 73* (eds Graham S, Lowe D), pp. 37–50. Pacific Section, Society of Economic Paleontologists and Mineralogists, Los Angeles, California.

Campbell KA, Francis D (1998) Miocene methane-seep carbonates of the East Coast Basin, North Island, New Zealand. *Geological Society of New Zealand Miscellaneous Publication*, **101A**, 61.

Campbell KA, Francis DA, Collins M (1999) Hydrocarbon seepage in the East Coast Basin convergent margin (Miocene–recent), New Zealand. *American Association of Petroleum Geologists, Pacific Section Convention Program*, **24**, 24.

Carlson C (1984a) Stratigraphic and structural significance of foliate serpentinite breccias, Wilbur Springs. In: *Depositional Facies of Sedimentary Serpentinite: Selected Examples from the Coast Ranges, California, Field Trip Guidebook, no. 3* (ed. Carlson C), pp. 108–12. Pacific Section, Society of Economic Paleontologists and Mineralogists, Tulsa, Oklahoma.

Carlson C (1984b) Descriptions of field trip stops 7, 8, and 9. In: *Depositional Facies of Sedimentary Serpentinite: Selected Examples from the Coast Ranges, California, Field Trip Guidebook, no. 3* (ed. Carlson C), pp. 117–21. Pacific Section, Society of Economic Paleontologists and Mineralogists, Tulsa, Oklahoma.

Carlson C (1984c) General geology of the northern Coast Ranges and the Wilbur Springs area. In: *Depositional Facies of Sedimentary Serpentinite: Selected Examples from the Coast Ranges, California, Field Trip Guidebook, no. 3* (ed. Carlson C), pp. 104–12. Pacific Section, Society of Economic Paleontologists and Mineralogists, Tulsa, Oklahoma.

Cavagna S, Clari P, Martire L (1999) The role of bacteria in the formation of cold seep carbonates: geological evidence from Monferrato (Tertiary, NW Italy). *Sedimentary Geology*, **126**, 253–70.

Clari P, Fornara L, Ricci B, Zuppi GM (1994) Methane-derived carbonates and chemosynthetic communities of Piedmont (Miocene, northern Italy): an update. *Geo-Marine Letters*, **14**, 201–9.

Clari P, Gagliardi C, Governa ME, Ricci B, Zuppi GM (1988) I Calcari di Marmorito: una testimonianza di processi diagenetici in

presenza di metano. *Bolletino Museo Regionale Scienze Naturali Torino*, **6**, 197–216.

Clari PA, Martire L (2000) Cold seep carbonates in the Tertiary of northwest Italy: evidence of bacterial degradation of methane. In: *Microbial Sediments* (eds Riding RE, Awramik SM), pp. 261–9. Springer-Verlag, Berlin.

Conti S, Fontana D (1999) Miocene chemoherms of the northern Appenines, Italy. *Geology*, **27**, 927–30.

Cook TL, Stakes DS (1995) Biogeological mineralization in deep-sea hydrothermal deposits. *Science*, **267**, 1975–9.

Coston J (1989) Carbonate diagenesis associated with abyssal brine seeps and chemosynthetic communities, Florida Escarpment, Gulf of Mexico. Masters Thesis. University of North Carolina, Chapel Hill, North Carolina.

Deines P (1980) The isotopic composition of reduced organic carbon. In: *Handbook of Environmental Isotope Geochemistry*, **Vol. 1** (eds Fritz P, Fontes JC), pp. 329–406. Elsevier, Amsterdam.

Derkachev AN, Bohrmann G, Greinert J (1999) Authigenic calcite and barite in sediments from Derugin Basin, Sea of Okhotsk. *American Association of Petroleum Geologists, Pacific Section Convention Program*, 26–7.

Dickinson WR (1971) Clastic sedimentary sequences deposited in shelf, slope, and trough settings, between magmatic arcs and associated trenches. *Pacific Geology*, **8**, 813–60.

Dickinson WR, Hopson CA, Saleeby JA (1996) Alternate origins of the Coast Range Ophiolite (California): introduction and implications. *GSA Today*, **6**, 1–10.

Donovan JJ, Snyder DA, Rivers ML (1993) An improved interference correction for trace element analysis. *Microbeam Analysis*, **2**, 23–8.

Ernst WG (1970) Tectonic contact between the Franciscan melange and the Great Valley sequence, crustal expression of a Late Mesozoic Benioff zone. *Journal of Geophysical Research*, **75**, 886–901.

Ferrell RE Jr, Aharon P (1994) Mineral assemblages occurring around hydrocarbon vents in the northern Gulf of Mexico. *Geo-Marine Letters*, **14**, 74–80.

Fouke BW (1994) *Deposition, diagenesis and dolomitization of Neogene Seroe Domi Formation coral reef limestones on Curaçao, Netherlands Antilles.* Publications Foundation for Scientific Research in the Caribbean Region, **133**, 1–182. The Hague, Amsterdam.

Fryer P (1992) A synthesis of Leg 125 drilling of serpentine seamounts on the Mariana and Izu-Bonin forearcs. In: *Proceedings of the Ocean Drilling Program, Scientific Results*, **125** (eds Fryer P, Pearce JA, Stokking LB, Ali JR, Arculus R, Ballotti DL, Bucke MM), pp. 593–614. Texas A&M University, College Station, Texas.

Gabb WM (1869) *Cretaceous and Tertiary fossils: palaeontology, v. II.* pp. 1–299. Geological Survey of California.

Gaillard C, Rio M, Rolin Y, Roux M (1992) Fossil chemosynthetic communities related to vents or seeps in sedimentary basins: the pseudobioherms of southeastern France compared to other world examples. *Palaios*, **7**, 451–65.

Given RK, Lohmann KC (1985) Derivation of the original isotopic composition of Permian marine cements. *Journal of Sedimentary Petrography*, **55**, 430–9.

Goedert JL, Campbell KA (1995) An Early Oligocene chemosynthetic community from the Makah Formation, northwestern Olympic peninsula. *Veliger*, **38**, 22–9.

Goldfinger C, Torres ME, Trehu AM (1999) Possible strike-slip fault source for Hydrate Ridge methane vents, Cascadia Margin. *American Association of Petroleum Geologists, Pacific Section Convention Program*, 29–30.

Greinert J, Suess E, Derkachev A, Obzhirov A, Baranov B, Winckler G (1999) Gas venting, biota and carbonate mineralization along the Sakhalin shear zone, Sea of Okhotsk. *American Association of Petroleum Geologists, Pacific Section Convention Program*, 30–31.

Haggerty JA (1987) Petrology and geochemistry of Neogene sedimentary rocks from Mariana forearc seamounts. Implications for emplacement of the seamounts. In: *Seamounts, Islands, and Atolls, Geophysical Monograph Series*, **43** (eds Keating BH, Fryer P, Batiza R, Boehlert GW), pp. 175–85. American Geophysical Union, Washington, D.C.

Haggerty JA (1991) Evidence from fluid seeps atop serpentine seamounts in the Marianas Forearc: clues for emplacement of the seamounts and their relationships to forearc tectonics. *Marine Geology*, **102**, 293–309.

Hamilton WB (1969) Mesozoic California and the underflow of Pacific mantle. *Geological Society of America Bulletin*, **80**, 2409–29.

Hannington MD, Jonasson IR, Herzig PM, Petersen S (1995) Physical and chemical processes of seafloor mineralization at mid-ocean ridges. In: *Seafloor Hydrothermal Systems: Physical, Chemical, Biological, and Geological Interactions, American Geophysical Union, Geophysical Monograph*, **91** (eds Humphris SE, Zierenberg RA, Mullineaux LS, Thomson RE), pp. 115–57. American Geophysical Union, Washington, D.C.

Hattori M, Oba T, Kanie Y, Akimoto K (1994) Authigenic carbonates collected from cold seepage area of Hatsushima Island, Sagami Bay, central Japan. *JAMSTEC Journal of Deep Sea Research*, **10**, 405–16.

Henry P, Mazzotti S, Lallemant S, Nakamura K-I, Kobayashi K (1999) Tectonically controlled fluid venting on the eastern Nankai margin: results of Kaiko-Tokai project. *American Association of Petroleum Geologists, Pacific Section Convention Program*, 31.

Hovland M, Judd AG (1988) *Seabed Pockmarks and Seepages: Impact on Geology, Biology and the Marine Environment*, pp. 1–293. Graham & Trotman, London.

Hovland M, Talbot MR, Qvale H, Olaussen S, Aasberg L (1987) Methane-related carbonate cements in pockmarks of the North Sea. *Journal of Sedimentary Petrology*, **57**, 881–92.

Howe B (1987) Tepee Buttes: a petrological, paleontological, paleoenvironmental study of Cretaceous submarine spring deposits. Masters Thesis. University of Colorado, Boulder, CO.

Humphris SE, Zierenberg RA, Mullineaux LS, Thomson RE, eds. (1995) *Seafloor Hydrothermal Systems: Physical, Chemical, Biological, and Geological Interactions, American Geophysical Union, Geophysical Monograph*, **91**, pp. 1–466. American Geophysical Union, Washington, D.C.

Ingersoll RV (1983) Petrofacies and provenance of Late Mesozoic forearc basin, northern and central California. *American Association of Petroleum Geologists Bulletin*, **67**, 1125–42.

Ingersoll RV, Dickinson WR (1981) Great Valley Group (sequence), Sacramento Valley, California. In: *Upper Mesozoic Franciscan Rocks and Great Valley Sequence, Central Coast Ranges, California (Annual Meeting Pacific Section SEPM Field Trips 1 and 4), Pacific Section, Society of Economic Paleontologists and Mineralogists*, **18** (ed. Frizzell V), pp. 1–33. SEPM, Bakersfield, California.

Jones DL, Bailey EH, Imlay RW (1969) Structural and stratigraphic significance of the *Buchia* zones in the Colyear Springs-Paskenta area California. *US Geological Survey Professional Paper*, **647-A**, 1–24, 5 plates.

Kauffman EG, Arthur MA, Howe B, Scholle PA (1996) Widespread venting of methane-rich fluids in Late Cretaceous (Campanian) submarine springs (Tepee Buttes), Western Interior Seaway, USA. *Geology*, **24**, 799–802.

Kelly SRA, Ditchfield PW, Doubleday PA, Marshall JD (1995) A Late Jurassic methane-seep limestone from the fore-arc basin

(Fossil Bluff Group) of Alexander Island, Antarctica. *Journal of Sedimentary Research*, **A65**, 274–82.

Klosterman SL, Sandy MR, Campbell KA (2001) A new occurrence of the Late Jurassic rhynchonellid *Cooperrhynchia* (Brachiopoda) from the Great Valley Group, California — confirming a cold-seep community association. *Geological Society of America, Abstracts with Programs*, **33**, A24.

Kohn MJ, Riciputi LR, Stakes D, Orange DL (1998) Sulfur isotope variability in biogenic pyrite: reflections of heterogeneous bacterial colonization? *American Mineralogist*, **83**, 1454–68.

Kulm LD, Suess E (1990) Relationship between carbonate deposits and fluid venting: Oregon accretionary prism. *Journal of Geophysical Research*, **95**, 8899–915.

Kulm LD, Suess E, Moore JC, Carson B, Lewis BT, Ritger SD, Kadko DC, Thornburg TM, Embley RW, Rugh WD, Massoth GJ, Langseth MG, Cochrane GR, Scammon RL (1986) Oregon subduction zone: venting, fauna, and carbonates. *Science*, **231**, 561–6.

Land LS (1989) The carbon and oxygen isotopic chemistry of surficial shallow marine carbonate cement and Quaternary limestone and dolomite. In: *Handbook of Environmental Isotope Geochemistry* (eds Fritz P, Fontes PC), pp. 191–217. Elsevier, Amsterdam.

Langseth MG, Moore JC (1990) Introduction to special section on the role of fluids in sediment accretion, deformation, diagenesis, and metamorphism in subduction zones. *Journal of Geophysical Research*, **95**, 8737–41.

Lawton JE (1956) Geology of the north half of the Morgan Valley quadrangle and the south half of the Wilbur Springs quadrangle, California. PhD Thesis. Stanford University, Stanford, CA.

Lécuyer C, Allemand P (1999) Modelling of the oxygen isotope evolution of seawater: implications for the climate interpretation of the $\delta^{18}O$ of marine sediments. *Geochimica et Cosmochimica Acta*, **63**, 351–61.

Lein AY, Gal'chenko VF, Pokrovskiy BG, Shabayeva IY, Chertkova LV, Miller YM (1989) Carbonate nodules produced by microbial gas hydrate oxidation in the Sea of Okhotsk. *Geokhimiya*, **10**, 1396–406.

Lewis KB, Marshall A (1996) Seep faunas and other indicators of methane-rich dewatering on New Zealand convergent margins. *New Zealand Journal of Geology and Geophysics*, **39**, 181–200.

Lewis DW, McConchie D (1994) *Analytical Sedimentology*, pp. 1–197. Chapman & Hall, New York.

Little CTS, Campbell KA, Herrington RJ (2002) Why did ancient chemosynthetic seep and vent assemblages occur in shallower water than they do today?: Comment. *International Journal of Earth Sciences*, **91**, 149–153.

Little CTS, Herrington RJ, Maslennikov VV, Morris NJ, Zaykov VV (1997) Silurian hydrothermal-vent community from the southern Urals, Russia. *Nature*, **385**, 146–8.

Little CTS, Herrington RJ, Maslennikov VV, Zaykov VV (1998) The fossil record of hydrothermal vent communities. In: *Modern Ocean Floor Processes and the Geological Record, Geological Society Special Publication*, **148** (eds Mills RA, Harrison K), pp. 259–70.Geological Society of London, London.

Lorenson TD, Naehr TH, Orange DL (1999) Gas seeps and associated gas hydrate of the Okhotsk Sea near Sakhalin Island, Russia, and Eel River basin, northern California – a comparison of gas and carbonate geochemistry. *American Association of Petroleum Geologists, Pacific Section Convention Program*, 36.

MacDonald IR, Boland GS, Baker JS, Brooks JM, Kennicutt MCII, Bidigare RR (1989) Gulf of Mexico hydrocarbon seep communities, II. Spatial distribution of seep organisms and hydrocarbons at Bush Hill. *Marine Biology*, **101**, 235–47.

Majima R, Tate Y, Shibasaki T (1996) In situ fossil chemosynthetic community found from the lower Pleistocene Kazusa Group, Yokohama City, central Japan. *Fossils*, **61**, 47–57.

Morse JW, Mackenzie FT (1990) *Geochemistry of Sedimentary Carbonates. Developments in Sedimentology*, **48**, pp. 1–707. Elsevier, Amsterdam.

Moxon IW (1990) Stratigraphy and structure of Upper Jurassic–Lower Cretaceous strata, Sacramento Valley. In: *Sacramento Valley Symposium and Guidebook, Pacific Section S.E.P.M.*, **65** (eds Ingersoll RV, Nilsen TH), pp. 5–29. SEPM, Los Angeles, California.

Naehr TH, Stakes DS (1999) Fluid flow and carbonate precipitation in the Eel River basin and Monterey Bay – two examples from the California Margin. *American Association of Petroleum Geologists, Pacific Section Convention Program*, 38.

Neumann AC, Paull CK, Commeau R, Chanton J, Martens C, Gardemal M, Trumbull W, Showers W (1988) Abyssal seep site cementation: West Florida Escarpment. *American Association of Petroleum Geologists Bulletin*, **72**, 228.

Orpin AR (1997) Dolomite chimneys as possible evidence of coastal fluid expulsion, uppermost Otago continental slope, southern New Zealand. *Marine Geology*, **138**, 51–67.

Pantin HM (1957) Fossiliferous concretions from the shelf southeast of Cape Campbell, New Zealand. *New Zealand Journal of Science and Technology, Section B*, **38**, 781–91.

Patterson WP, Walter LM (1994) Depletion of ^{13}C in seawater CO_2 on modern carbonate platforms — significance for the carbon isotopic record of carbonates. *Geology*, **22**, 885–8.

Paull CK, Chanton JP, Martens CS, Fullagar PD, Neumann AC, Coston JA (1991) Seawater circulation through the flank of the Florida Platform: evidence and implications. *Marine Geology*, **102**, 265–79.

Paull CK, Chanton JP, Neumann AC, Coston JA, Martens CS (1992) Indicators of methane-derived carbonates and chemosynthetic organic carbon deposits: examples from the Florida Escarpment. *Palaios*, **7**, 361–75.

Peckmann J, Campbell KA, Walliser OH, Reitner J (2000) A growing Paleozoic record of hydrocarbon seep deposts. *EOS Transactions, Fall Meeting Supplement, American Geophysical Union*, **81**, OS61B–05.

Peckmann J, Gischler E, Oschmann W, Reitner J (2001a) An Early Carboniferous seep community and hydrocarbon-derived carbonates from the Harz Mountains, Germany. *Geology*, **29**, 271–4.

Peckmann J, Reimer A, Luth U, Luth C, Hansen BT, Heinicke C, Hoefs J, Reitner J (2001b) Methane-derived carbonates and authigenic pyrite from the northwestern Black Sea. *Marine Geology*, **177**, 129–50.

Peckmann J, Thiel V, Michaelis W, Clari P, Gaillard C, Martire L, Reitner J (1999a) Cold seep deposits of Beauvoisin (Oxfordian, southeastern France) and Marmorito (Miocene, northern Italy): microbially induced authigenic carbonates. *International Journal of Earth Sciences*, **88**, 60–75.

Peckmann J, Walliser OH, Riegel W, Reitner J (1999b) Signatures of hydrocarbon venting in a Middle Devonian carbonate mound (Hollard Mound) at the Hamar Laghdad (Antiatlas, Morocco). *Facies*, **40**, 281–96.

von Rad U, Rösch H, Berner U, Geyh M, Marchig V, Schulz H (1996) Authigenic carbonates derived from oxidized methane vented from the Makran accretionary prism off Pakistan. *Marine Geology*, **136**, 55–77.

Rasmussen B (2000) Filamentous microfossils in a 2,235-million-year-old volcanogenic massive sulfide deposit. *Nature*, **405**, 676–9.

Rio M, Roux M, Renard M, Schein E (1992) Chemical and isotopic features of present day bivalve shells from hydrothermal vents or cold seeps. *Palaios*, **7**, 351–60.

Ritger S, Carson B, Suess E (1987) Methane-derived authigenic carbonates formed by subduction-induced pore-water expulsion along Oregon/Washington margin. *Geological Society of America Bulletin*, **98**, 147–56.

Roberts HH, Aharon P (1994) Hydrocarbon-derived carbonate buildups of the northern Gulf of Mexico: a review of submersible investigations. *Geo-Marine Letters*, **14**, 135–48.

Roberts HH, Aharon P, Carney R, Larkin J, Sassen R (1990) Sea floor responses to hydrocarbon seeps, Louisiana continental slope. *Geo-Marine Letters*, **10**, 232–43.

de Ronde CEJ, Ebbesen TW (1996) 3.2 b.y. of organic compound formation near sea-floor hot springs. *Geology*, **24**, 791–4.

Sakai H, Gamo T, Ogawa Y, Boulegue J (1992) Stable isotopic ratios and origins of the carbonates associated with cold seepage at the eastern Nankai Trough. *Earth and Planetary Science Letters*, **109**, 391–404.

Sample JC (1996) Isotopic evidence from authigenic carbonates for rapid upward fluid flow in accretionary wedges. *Geology*, **24**, 897–900.

Sample JC, Kopf A (1995) Isotope geochemistry of syntectonic carbonate cements and veins from the Oregon margin (ODP Leg 146): implications for the hydrogeologic evolution of the accretionary wedge. In: *Proceedings of the Ocean Drilling Program, Scientific Results*, **146**(1) (eds Carson B, Westbrook GK, Musgrave RJ, Suess E), pp. 137–48. Texas A&M University, College Station, TX.

Sample JC, Reid MR (1998) Contrasting hydrogeologic regimes along strike-slip and thrust faults in the Oregon convergent margin: evidence from chemistry of syntectonic carbonate cements and veins. *Geological Society of America Bulletin*, **110**, 48–59.

Sample JC, Reid MR, Tobin HJ, Moore JC (1993) Carbonate cements indicate channeled fluid flow along a zone of vertical faults at the deformation front of the Cascadia accretionary wedge (northwest US coast). *Geology*, **21**, 507–10.

Sandy MR, Campbell KA (1994) A new rhynchonellid brachiopod genus from Tithonian (upper Jurassic) cold-seep deposits of California and its paleoenvironmental setting. *Journal of Paleontology*, **68**, 1243–52.

Savard MM, Beauchamp B, Veizer J (1996) Significance of aragonite cements around Cretaceous marine methane seeps. *Journal of Sedimentary Research*, **66**, 430–8.

Schumacher D, Abrams MA, eds. (1996) *Hydrocarbon Migration and its Near-Surface Expression. American Association of Petroleum Geologists Memoir*, **66**, 1–446.

Shibasaki T, Majima R (1997) A fossil chemosynthetic community from outer shelf environment of the Middle Pleistocene Kakinokidai Formation, Kazusa Group in Boso Peninsula, Chiba Prefecture, central Japan. *Journal of the Geological Society of Japan*, **103**, 1065–80.

Shillito B, Lechaire J-P, Goffinet G, Gaill F (1995) Composition and morphogenesis of the tubes of vestimentiferan worms. In: *Hydrothermal Vents and Processes, Geological Society Special Publication*, **87** (eds Parson LM, Walker CL, Dixon DR), pp. 295–302. Geological Society of London, London.

Simoneit BRT, Lonsdale PF, Edmond JM, Shanks WC III (1990) Deep-water hydrocarbon seeps in Guaymas Basin, Gulf of California. *Applied Geochemistry*, **5**, 41–9.

Southward E (1991) Three new species of Pogonophora, including two vestimentiferans, from hydrothermal sites in the Lau back-arc basin (southwest Pacific Ocean). *Journal of Natural History*, **25**, 859–81.

Stakes DS, Orange D, Paduan JB, Salamy KA, Maher N (1999) Cold-seeps and authigenic carbonate formation in Monterey Bay, California. *Marine Geology*, **159**, 93–109.

Stanton TW (1895) Contributions to the Cretaceous paleontology of the Pacific coast: the fauna of the Knoxville beds. *US Geological Survey Bulletin*, **133**, 1–132.

Suchecki RK (1984) Facies history of the Upper Jurassic–Lower Cretaceous Great Valley Sequence: response to structural development of an outer-arc basin. *Journal of Sedimentary Petrography*, **54**, 170–91.

Suess E, Bohrmann G, von Huene R, Linke P, Wallman K, Lammers S, Sahling H (1998) Fluid venting in the eastern Aleutian subduction zone. *Journal of Geophysical Research*, **103**, 2597–614.

Suess E, Whiticar MJ (1989) Methane-derived CO_2 in pore fluids expelled from the Oregon subduction zone. *Palaeogeography, Palaeoclimatology, Palaeoecology*, **71**, 119–36.

Terzi C, Aharon P, Ricci Lucchi F, Vai GB (1994) Petrography and stable isotope aspects of cold-vent activity imprinted on Miocene-age 'calcari a *Lucina*' from Tuscan and Romagna Appenines, Italy. *Geo-Marine Letters*, **14**, 177–84.

Thiel V, Peckmann J, Seifert R, Wehrung P, Reitner J, Michaelis W (1999) Highly isotopically depleted isoprenoids: molecular markers for ancient venting. *Geochimica et Cosmochimica Acta*, **63**, 3959–66.

Van Dover CL (2000) *The Ecology of Deep-Sea Hydrothermal Vents*, pp. 1–424. Princeton University Press, Princeton.

Veizer J (1983) Trace elements and isotopes in sedimentary carbonates. In: *Carbonates, Mineralogy and Chemistry, Mineralogical Society of America, Reviews in Mineralogy*, **11** (ed. Reeder RJ), pp. 265–99. Mineralogical Society of America, Washington, D.C.

Wilkin RT, Barnes HL (1996) Pyrite formation by reactions of iron monosulfides with dissolved inorganic and organic sulfur species. *Geochimica et Cosmochimica Acta*, **60**, 4167–79.

Wilkin RT, Barnes HL (1997) Formation processes of framboidal pyrite. *Geochimica et Cosmochimica Acta*, **61**, 323–39.

Zonenshayn LP, Murdmaa IO, Baranov BV, Kuznetsov AP, Kuzin VS, Kuz'min MI, Avdeyko GP, Stunzhas PA, Lukashin VN, Barash MS, Valyashko GM, Demina LL (1987) An underwater gas source in the Sea of Okhotsk west of Paramushir Island. *Oceanology*, **27**, 598–602.